# Impact of Ural Blocking on Winter Warm Arctic–Cold Eurasian Anomalies. Part II: The Link to the North Atlantic Oscillation

DEHAI LUO,[a] YIQING XIAO,[a,b,c] YINA DIAO,[b] AIGUO DAI,[d,e] CHRISTIAN L. E. FRANZKE,[f,g] AND IAN SIMMONDS[h]

[a] *RCE-TEA, Institute of Atmospheric Physics, Chinese Academy of Sciences, Beijing, China*
[b] *Physical Oceanography Laboratory, Qingdao Collaborative Innovation Center of Marine Science and Technology, Ocean University of China, Qingdao, China*
[c] *Shanxi Meteorological Observatory, Xi'an, China*
[d] *Department of Atmospheric and Environmental Sciences, University at Albany, State University of New York, Albany, New York*
[e] *National Center for Atmospheric Research, Boulder, Colorado*
[f] *Meteorological Institute, University of Hamburg, Hamburg, Germany*
[g] *Center for Earth System Research and Sustainability (CEN), University of Hamburg, Hamburg, Germany*
[h] *School of Earth Sciences, University of Melbourne, Melbourne, Victoria, Australia*

(Manuscript received 26 August 2015, in final form 1 March 2016)

ABSTRACT

In Part I of this study, the Ural blocking (UB)-induced amplification role of winter warm Arctic–cold Eurasian (WACE) anomalies has been examined. It was found that the long-lived UB together with the positive North Atlantic Oscillation ($NAO^+$) significantly contributes to the amplification of the WACE pattern. The present study examines how the UB variability affects quasi-biweekly WACE (QB-WACE) anomalies and depends on the $NAO^+$ and North Atlantic conditions by classifying the UB based on a case study of a cold event that occurred over southern China in January 2008. A composite analysis during 1979–2013 shows that the QB-WACE anomalies associated with the UB that often occur with the $NAO^+$ are strong and influenced by the North Atlantic jet (NAJ) and zonal wind strengths over Eurasia. For $NAO^+$-related UB, the QB-WACE anomaly depends strongly on the location of UB, and the UB anomalies lag the $NAO^+$ by approximately 4–7 days.

The strength of the NAJ determines whether the combined $NAO^+$ and UB anomalies exhibit a negative East Atlantic/West Russia ($EA/WR^-$) pattern, while the region of weak zonal winds over Eurasia and the zonal extent of the NAJ dominate the location of UB. For southward-, eastward-, and westward-displaced UBs associated with a strong NAJ, the $NAO^+$ favors the UB with a southward-displaced QB-WACE anomaly through wave train propagation like an $EA/WR^-$ pattern. Eastward- and southward-displaced UB anomalies induce similarly displaced cold anomalies with intrusion into southern China. However, for a northward-displaced UB, this happens without pronounced $EA/WR^-$ patterns because of a weak NAJ and is accompanied by a northward-displaced QB-WACE anomaly.

## 1. Introduction

In Luo et al. (2016, hereafter Part I) the regression analysis of the winter (DJF)-mean 500-hPa geopotential height anomalies revealed that the winter sea ice loss over the Barents and Kara Seas (BKS) is associated with the Ural blocking (UB) pattern and the positive North Atlantic Oscillation ($NAO^+$) and is followed by a winter-mean warm Arctic–cold Eurasian (WACE) temperature pattern, while the overall atmospheric response to arctic sea ice loss resembles a negative Arctic response oscillation ($ARO^-$) pattern. The sea ice loss over the North American high-latitude (NAH) region (Baffin and Hudson Bay, Davis Strait, and Labrador Sea) corresponds to a negative-phase NAO ($NAO^-$)-like pattern and is followed by high-latitude cold anomalies over Eurasia. Thus, the role of the arctic sea ice loss in different sectors during the outbreak of Eurasian cold events is likely different. To some extent, the

*Corresponding author address*: Dr. Dehai Luo, RCE-TEA, Institute of Atmospheric Physics, Chinese Academy of Sciences, Huayanli 40, Chaoyang District, Beijing 100029, China.
E-mail: ldh@mail.iap.ac.cn

DOI: 10.1175/JCLI-D-15-0612.1

ARO$^-$-like pattern associated with the overall arctic sea ice loss may be explained as a superimposition of the NAO$^-$-like pattern associated with the NAH sea ice reduction and the UB pattern together with the NAO$^+$ that is related to the BKS sea ice loss. In this mode, the UB pattern is a very important component that constitutes the main body of the ARO$^-$-like pattern. These results are different from previous investigations (Honda et al. 2009; Petoukhov and Semenov 2010; Liu et al. 2012; Zhang et al. 2012; Cohen et al. 2012, 2014; Screen and Simmonds 2013a,b, 2014; Tang et al. 2013; Mori et al. 2014; Sato et al. 2014; Simmonds and Govekar 2014).

On the other hand, as revealed in Luo et al. (2015a,b, 2016), the UB events are more persistent during the period 2000–13 (P2) than during 1979–99 (P1) because of weaker middle-to-high-latitude westerly winds induced by the BKS sea ice loss, and the blocking days exhibit an upward trend during P2. Long-lived UB patterns can induce an additional arctic warming and Eurasian cooling because of the warm and cold advection associated with the UB; thus, they can amplify the preexisting warming over the BKS to strengthen the winter-mean WACE pattern. Further results of Luo et al. (2016) also indicate that the NAO$^+$ (NAO$^-$) corresponds to a higher (lower) UB frequency (days). Thus, it is necessary to consider the phase of the NAO and its variability in order to understand the cause of the variations of the UB frequency and the associated DJF-mean WACE anomaly. Because the UB and NAO events are of quasi-biweekly (10–20 day) time scales, in this paper we focus on examining the impact of UB and NAO events on the quasi-biweekly WACE (QB-WACE) anomaly, which is referred to in Part I. Changes in the QB-WACE anomaly can help us understand the variations in winter-mean WACE.

As revealed by the two UB events that occurred in January 2008 (see section 3), the variation of the QB-WACE anomaly depends strongly on the location of the UB pattern. Because the strength of the North Atlantic jet (NAJ) can affect the location and strength of downstream blocking during the NAO$^+$ episodes (Luo et al. 2015b), it is important to establish a possible link between the NAO$^+$, North Atlantic conditions, and the UB pattern. Such an investigation will deepen our understanding of the physical mechanism of the QB-WACE variability associated with UB events, which is the main purpose of this paper. In this paper, we consider only the link of the QB-WACE anomaly with the blocking and NAO on a time scale of about 10 days. In addition, eddy–mean flow interaction theory and wave activity flux analysis are used to indicate that the energy source of the UB establishment mainly comes from the North Atlantic basin through the energy dispersion or the wave train propagation similar to a negative phase East Atlantic/West Russia (EA/WR$^-$) pattern of quasi-stationary waves generated in the North Atlantic region. Thus, it is also important to examine which factors affect the planetary wave train generation and its relationship with the NAO$^+$ and UB patterns.

This paper is organized as follows: In section 2, we describe the data and methodology. The eddy–mean flow interaction equation and the wave activity flux formula used in this paper are described in appendixes A and B. In section 3, a case study of cold temperatures and snow–ice weather that occurred over southern China in January 2008 is presented to help classify the UB patterns associated with cold events. In section 4, we describe a composite analysis of NAO$^+$-related UB events during 1979–2013 in terms of the classification of UB patterns. In section 5, the physical mechanisms of the UB initiation and its variability are examined. In section 6, we examine what affects the planetary wave train associated with the variation of the UB location. Conclusions and discussion are presented in section 7.

## 2. Data and methodology

Here we used the daily ERA-Interim data (Dee et al. 2011), which has also been used in Part I. The daily NAO index used here is the same as that described in Part I. Here, two metrics for the definition of an NAO event are used. First, an NAO$^+$ (NAO$^-$) event is defined based on its daily NAO index that must at least attain $+1.0$ ($-1.0$) standard deviations (STDs) from zero for at least three consecutive days. This is referred to as the 1.0-STD case. The second definition is related but less restrictive, and an NAO$^+$ (NAO$^-$) event is defined to have taken place if the daily NAO index is $\geq +0.5$ ($\leq -0.5$) STDs for at least three consecutive days (the 0.5-STD case). The lifetime of an NAO$^+$ (NAO$^-$) event is defined as the time that the daily NAO index increases (decreases) from zero to its maximum (minimum) value and then decreases (increases) back to zero, rather than the time that the NAO index remains above the STD. In this study, the classification of the UB patterns is based on the selected 54 UB events during 1979–2013 in Part I.

Here, the eddy-induced streamfunction tendency method in the eddy–mean flow interaction equation, which is described in appendix A, is used to determine whether the UB is formed through the forcing of synoptic-scale eddies over Eurasia if the NAO or blocking is considered a time-mean flow (Hoskins et al. 1983). Then, the wave activity flux vector described in appendix B is calculated to demonstrate whether the UB arises from the planetary wave train propagation across Europe. By calculating the eddy-induced streamfunction tendency field and wave activity flux vector, it is easy to identify where the energy source

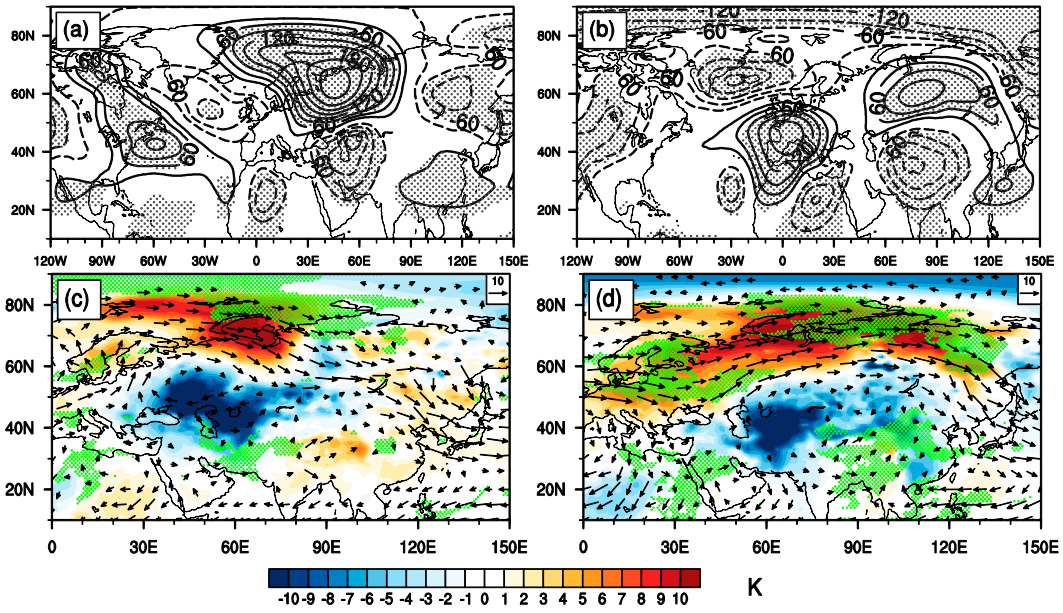


FIG. 1. Time-mean anomalies of (a),(b) 500-hPa geopotential height (gpm; contour interval = 30 gpm) and (c),(d) surface air temperature (colors) and areas with significant precipitation (green shading) for the two UB events averaged (left) from 30 December 2007 to 12 January 2008 (event 1) and (right) from 17 to 30 January 2008 (event 2). In (a),(b), the gray stippling denotes the region above the 95% confidence level based on a two-sided Student's $t$ test and the red arrow denotes the anomaly vector of time-mean 850-hPa horizontal winds. In (c),(d), the dotted regions are above the 95% confidence level based on a two-sided Student's $t$ test and the dark arrows denote the time-mean 850-hPa total wind vector. Area with precipitation anomalies above the 95% confidence level are shaded in green.

of the UB formation comes from and whether the UB is related to North Atlantic circulations.

## 3. A case study of the January 2008 cold event over Eurasia and the classification of UB events

### *a. Large-scale circulation features*

We present a cold event to show that the location of the UB pattern is important for the QB-WACE variability and the occurrence region of the associated cold anomaly. Thus, it is reasonable to classify the UB pattern in terms of its zonal and meridional positions. To perform a classification of the winter UB events during 1979–2013, it is useful to examine the large-scale structure of the cold event that occurred over southern China in January 2008 because it is associated with the UB pattern. The persistent cold temperatures and severe snow–ice weather over southern China in January 2008 are typical examples of extreme cold events over East Asia (Wen et al. 2009; Han et al. 2011; Bueh et al. 2011). Two blocking events occurred over the Eurasian continent from 30 December 2007 to 13 January 2008 (event 1) and from 15 to 31 January 2008 (event 2).

To see the difference between events 1 and 2, we show time-mean anomalies of 500-hPa geopotential height and surface air temperature (SAT) over the Eurasian continent for event 1 averaged from 30 December 2007 to 12 January 2008 and for event 2 averaged from 17 to 30 January 2008 in Fig. 1. The UB anomaly exhibits a positive-over-negative dipole structure in the meridional direction for both events. This dipole anomaly is referred to as the UB dipole anomaly, which is located more eastward and southward for event 2 than for event 1, even though it is relatively weak for event 2 (Fig. 1b). In particular, for event 1 the negative-over-positive (NOP) dipole pattern over the North Atlantic is tilted toward the southwest–northeast (SW–NE) direction so that its combination with the UB anomaly generates an arching wave train from the North Atlantic to the Ural region (Fig. 1a). This wave train resembles an EA/WR$^-$ pattern (Barnston and Livezey 1987; Lim 2015) with a strong anticyclonic circulation over western Russia west of 60°E. Such a wave train structure is less evident for event 2 because the NOP dipole pattern in the North Atlantic basin and western Europe is aligned along the southeast–northwest (SE–NW) direction (Fig. 1b). The eastward movement of the intensified NOP dipole anomaly in the North Atlantic basin is in accord with the eastward displacement of the UB dipole anomaly.

For the two UB events, the SAT anomaly field exhibits a dipole structure with a warm anomaly in the

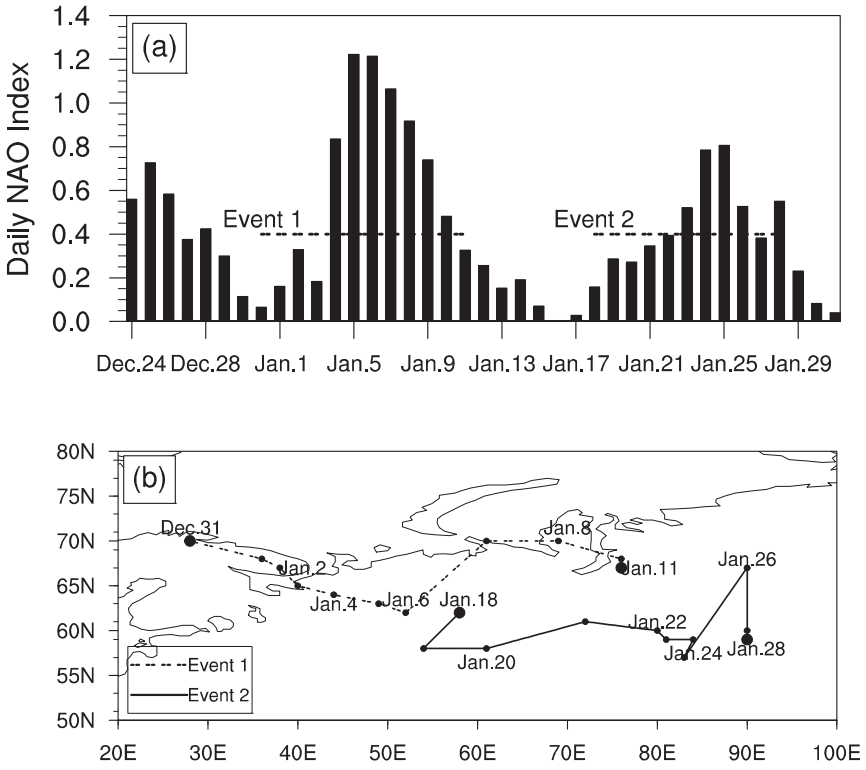


FIG. 2. (a) Time evolution of the daily NAO index in January 2008 and (b) the trajectory of the center of the maximum amplitude of the UB event, in which the dashed lines in (a) represent the two UB events, events 1 and 2, as shown in Fig. 1, whereas in (b) the dashed (solid) line denotes event 1 (event 2).

high latitudes and subarctic region and a cold anomaly over the midlatitude Eurasian continent. This dipole SAT anomaly is referred to as the QB-WACE anomaly, although it has changed from event 1 to event 2 and its cold anomaly does not cover the whole of Eurasia. In this QB-WACE anomaly, the cold anomaly of event 1 has a narrower region (30°–90°E) that spans eastern Europe, western Russia, the Black Sea, the Caspian Sea, the Ural Mountains, and western Siberia (Fig. 1c), while event 2 has a more widespread cold anomaly region (50°–120°E) from the east of the Caspian Sea to central Siberia that spreads farther east and south and spans Iran, Afghanistan, Pakistan, and large portions of China, including southern China. Event 2 also has a more widespread warm anomaly in the subarctic region that spreads farther east than event 1. This indicates that the QB-WACE pattern can be significantly influenced by the position of the UB. In some sense, the strong and wide cold anomaly observed during event 2 can be explained as the continuous accumulation and extension of cold air of event 1 into event 2 that appeared rapidly after the decay of event 1. The time-mean 850-hPa horizontal wind vector (arrows in Figs. 1c,d) and its anomaly vector (the nature of which can be estimated from Figs. 1a,b) show that the cold air from northern China can reach southern China for event 2 through cold temperature advection induced by northerlies (Figs. 1b,d). The intensified southern branch trough of the plateau trough near 85°E as seen in the total height field from 19 to 25 January (not shown) brings more moisture into southwestern and southern China through southwesterly winds. This leads to persistent low temperatures and snow–ice weather over southern China from 15 to 31 January 2008 (Wen et al. 2009; Bueh et al. 2011; Han et al. 2011), but this is not the case for event 1 (Figs. 1a,c).

### b. *The connection of the two blocking events in January 2008 to NAO events*

As seen in Fig. 1, the NOP dipole anomalies in the North Atlantic correspond to $NAO^+$ patterns for both events 1 and 2, although their zonal locations are significantly different and the axes of the NOP dipole anomalies differ. The positive NAO index is smaller for event 2 (Fig. 2a), while the $NAO^+$ dipole anomaly is stronger for event 2 (Figs. 1a,b). It should be pointed out that the daily NAO index cannot precisely reflect the strength and location of localized $NAO^+$ dipole anomalies, which vary in time and zonal direction. This is

because the daily NAO index is constructed by projecting the daily 500-hPa geopotential height anomalies over the Northern Hemisphere onto the loading pattern of the NAO (Barnston and Livezey 1987). On the other hand, it is also difficult to derive the exact evolution of individual UB and $NAO^+$ events in terms of the daily NAO index because it cannot differentiate the spatial structures of UB and $NAO^+$ patterns, even though it can be used to select the $NAO^+$ events during the winters of 1979–2013.

Before classifying the UB pattern, we should look at the movements of the UB for event 1 and event 2 to understand why their zonal positions are different. Here, we define the position of the maximum amplitude of the large-scale anticyclonic anomaly over Eurasia as the blocking position, and we track these, as shown in Fig. 2b. It is found that for both events the maxima move eastward following the background westerly winds. Because event 2 (event 1) originates from the Ural region (European continent), their time-mean positions are different, although they are both associated with an $NAO^+$ event, in which event 2 (Fig. 1b) is located more eastward and southward (Fig. 1a). This motivates us to classify the UB patterns into two types: northward- and southward-displaced (westward- and eastward-displaced) blocking patterns in the meridional (zonal) location of the UB events. Based on this classification, we focus on examining the impact of different locations of UB anomalies on the QB-WACE pattern and looking for what factors determine the different position of UB dipole anomalies rather than on examining the synoptic process and mechanism that lead to the persistent low temperature and snow–ice weather over China.

## 4. Composite analyses

As noted above, the variation of the UB events is related to the phase of the NAO. Thus, to understand the relationship between the UB and NAO patterns, it is useful to pick NAO events during the 1979–2013 winters according to the two standards of the above NAO definition before a composite analysis is made. It is found that during the winters of 1979–2013, there are 62 $NAO^+$ and 30 $NAO^-$ events for the 1.0-STD case and 120 $NAO^+$ and 54 $NAO^-$events for the 0.5-STD case. If a UB event occurs completely within the life cycle of an NAO event, then the UB event is considered to be associated with the NAO event and referred to as an NAO-related UB event hereafter. The UB event is defined to be related to an $NAO^+$-to-$NAO^-$ event if it occurs within a life cycle from the beginning of an $NAO^+$ event to the end of an $NAO^-$ event. As in Part I, we detect 54 UB events during the winters (DJF) of 1979–2013 according to the TM index from Tibaldi and Molteni (1990). The numbers of these UB events associated with $NAO^+$, $NAO^-$, $NAO^+$-to-$NAO^-$, and neutral NAO (non-NAO) events during 1979–2013 are shown in Fig. 3 for 1.0- and 0.5-STD cases.

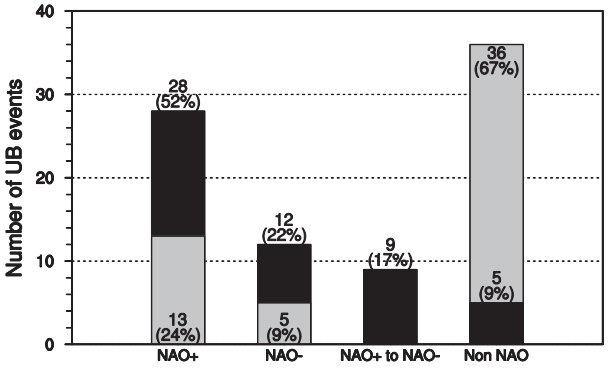


FIG. 3. The number and percentage of UB events associated with different types of NAO events based on 1.0 (gray) and 0.5 (black) STDs during the winters (DJF) of 1979–2013 using ERA-Interim data. The neutral NAO event is simply referred to as a non-NAO event.

For the 1.0-STD case, there are 13 $NAO^+$- and 5 $NAO^-$-related UB events, while 36 UB events are unrelated to NAO events. For this case, 21% (17%) of 62 $NAO^+$ (30 $NAO^-$) events are related to UB events. In other words, 24% (9%) of 54 UB events are related to $NAO^+$ ($NAO^-$) events. For the 0.5-STD case, there are 28 $NAO^+$- and 12 $NAO^-$-related UB events, although 9 UB events are related to $NAO^+$-to-$NAO^-$ events and 5 UB events are not related to any NAO events. For this case, 23% (22%) of 120 $NAO^+$ (54 $NAO^-$) events are related to UB events. This also corresponds to the case that 52% (22%) of 54 UB events are related to $NAO^+$ ($NAO^-$) events.

For the 0.5-STD case, we found that there are 15 (19.7%) $NAO^+$ and 6 (18.2%) $NAO^-$ cases related to UB during P1 and 13 (29.5%) $NAO^+$ and 6 (28.6%) $NAO^-$ cases related to UB during P2. Thus, there is a large increase in the event numbers of UB-related $NAO^+$ and $NAO^-$ events from P1 to P2. Although the event number of the UB-related $NAO^+$ events is almost the same as that of the UB-related $NAO^-$ events for each one of both P1 and P2, the mean lifetime of the UB events is different between P1 and P2 for the two phases of the NAO. For example, for the $NAO^+$ ($NAO^-$) the mean lifetime of the UB events is 8.6 (7.3) days during P1 but increases to 10.3 (8.2) days during P2. Thus, the mean lifetime of the UB events is longer during the $NAO^+$ than during the $NAO^-$, and this difference is more evident during P2 than during P1. This confirms our finding in Part I (Fig. 16 therein). This also

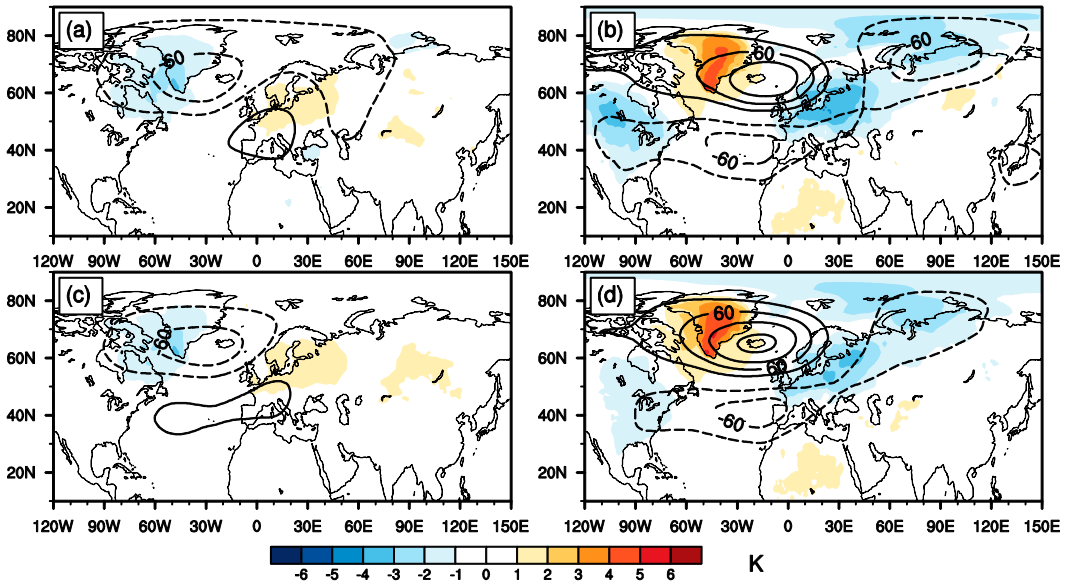


FIG. 4. Time-mean anomalies of 500-hPa geopotential height (gpm; contour interval = 30 gpm) and detrended surface air temperature (K; colors) averaged from lag −5 to 5 days of (a),(c) $NAO^+$ events (49 and 97 cases, respectively) and (b),(d) $NAO^-$ events (25 and 43 cases, respectively) without UB for (a),(b) 1.0- and (c),(d) 0.5-STD cases during winters of 1979–2013. Lag 0 denotes the day that the NAO amplitude is largest. In (a),(b), the contours denote the regions above the 95% confidence level based on a two-sided Student's *t* test, and the red (blue) denotes the positive (negative) temperatures above the 95% confidence level based on a two-sided Student's *t* test.

indicates that the method used to select UB and NAO events is appropriate, and thus, we may classify the UB and NAO patterns in terms of selected UB and NAO events. In this paper, because the $NAO^-$-related UB events are less frequent, we do not classify the $NAO^-$-related UB patterns for a 0.5-STD case. Instead, we classify only the $NAO^+$-related UB events.

### a. *Impact of NAO events without UB on temperature anomalies over Eurasia*

To clearly understand the role of NAO events with UB in the WACE pattern, it is useful to first examine the impact of NAO events without UB (UB-unrelated NAO events) on temperature anomalies over Eurasia. For the two phases of the NAO, we show the time-mean 500-hPa geopotential height and SAT anomalies of UB-unrelated NAO events averaged from lag −5 to 5 days in Fig. 4 for both the 1.0- and 0.5-STD cases. The results for the time average from lag −10 to 10 days are very similar (not shown).

It is seen that for the two phases of NAO events without UB the detrended SAT anomaly has almost the same pattern, although the NAO pattern is slightly different between the 1.0- and 0.5-STD cases (Fig. 4). For $NAO^+$ events, weak warm (cold) anomalies occur over the Eurasian continent (Greenland) (Figs. 4a,c), while weak cold (warm) anomalies emerge over northern Europe and the BKS (Greenland) for $NAO^-$ events (Figs. 4b,d). Thus, although the $NAO^-$ pattern corresponds to cold anomalies over the BKS region, there is a nonlinear response in the sense that warm (or any) anomalies do not appear over the BKS region for the $NAO^+$ pattern if UB events are absent. Taken together, this means that the presence of any phase of the NAO pattern cannot generate warming over the BKS region if UB events are absent. However, the result becomes completely different if UB events are present, as we shall see below.

### b. *Impact of NAO-related UB events on QB-WACE patterns*

To examine the different impacts of the UB events associated with different NAO regimes on the QB-WACE pattern, we consider the two cases of our NAO event definitions (1.0 and 0.5 STDs). Figure 5 shows the time-mean anomalies of 500-hPa geopotential height and SAT averaged from lag −5 to 5 days for UB events associated with $NAO^+$, $NAO^-$, and neutral NAO events for the 1.0-STD case (where lag 0 denotes the day of the UB peak), while the results of UB events associated with $NAO^+$, $NAO^-$, $NAO^+$-to-$NAO^-$, and neutral NAO events are shown in Fig. 6 for the 0.5-STD case.

Clearly, the structure of the QB-WACE anomaly depends on whether the UB event is related to the NAO. For a 1.0-STD case (Fig. 5), the warm (cold) anomalies over the Arctic (Eurasia) are strong for

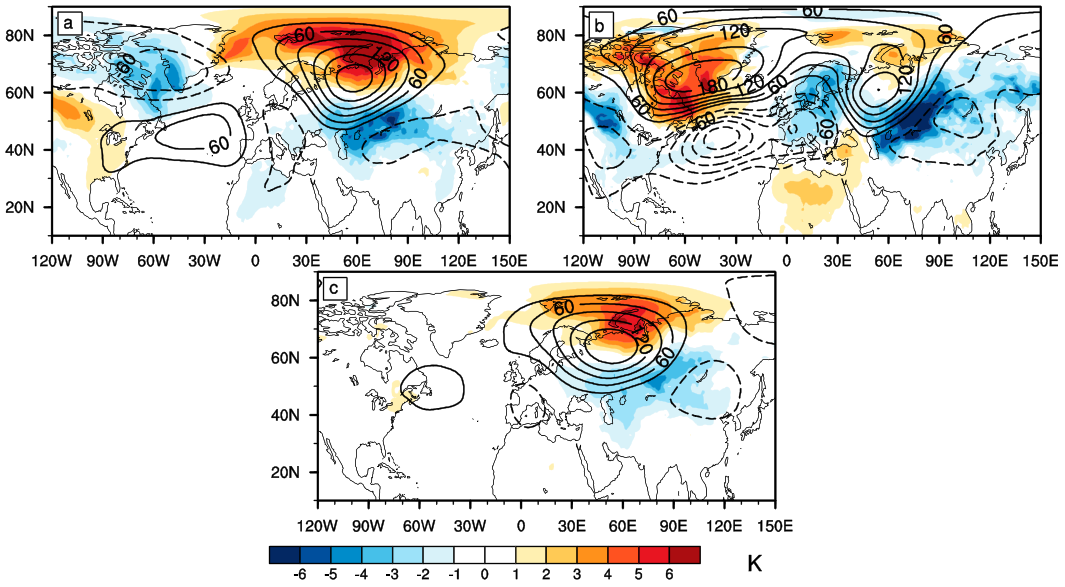


FIG. 5. Time-mean anomalies of 500-hPa geopotential height (gpm; contour interval = 30 gpm) and surface air temperature (K; colors) for the UB events from lag −5 to 5 days for (a) $NAO^+$ (13 cases), (b) $NAO^-$ (5 cases), and (c) neutral NAO (36 cases) events for a 1.0-STD case during winters of 1979–2013. Lag 0 denotes the day when the UB peaks. In (a)–(c), the contours denote the regions above the 95% confidence level based on a two-sided Student's *t* test, and the red (blue) denotes the positive (negative) SAT region above the 95% confidence level based on a two-sided Student's *t* test.

$NAO^+$-related UB events so as to produce an intense QB-WACE anomaly pattern (Fig. 5a). For $NAO^-$-related UB events, the arctic warming is relatively weak, while the cold anomalies over Eurasia are strong and widespread (Fig. 5b). However, we should bear in mind here that, even though the cold anomalies are strong, we are dealing with only five cases. As we will see below, the strength and area of Eurasian cold anomalies are

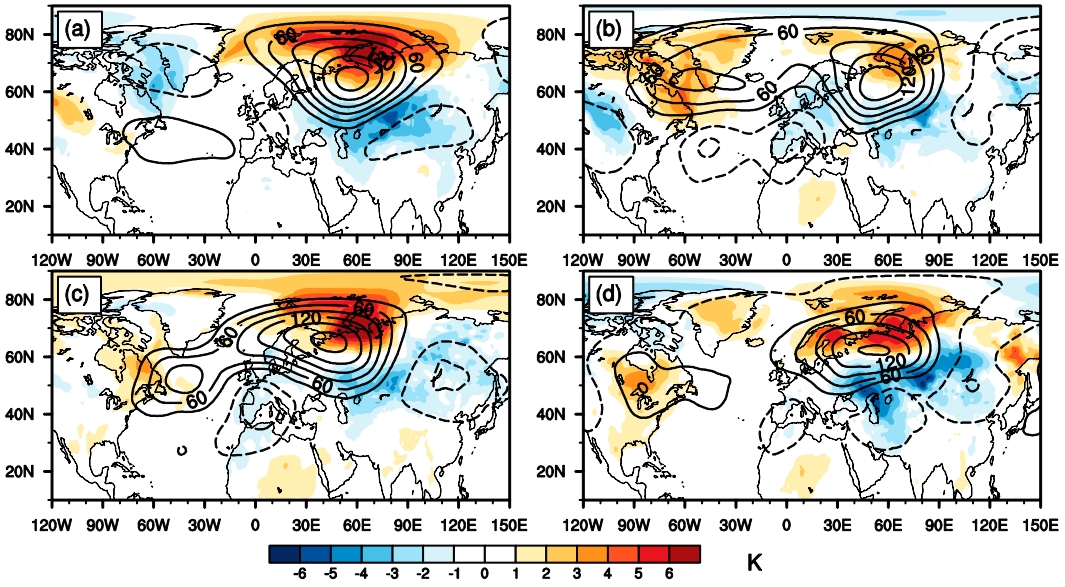


FIG. 6. Time-mean anomalies of 500-hPa geopotential height (gpm; contour interval = 30 gpm) and surface air temperature (K; colors) for the UB events averaged from lag −5 to 5 days associated with (a) $NAO^+$ (28 cases), (b) $NAO^-$ (12 cases), (c) $NAO^+$-to-$NAO^-$ (9 cases), and (d) neutral NAO (5 cases) events for a 0.5-STD case during winters of 1979–2013. Lag 0 denotes the day when the UB peaks. In (a)–(d), the contours denote the regions above the 95% confidence level based on a two-sided Student's *t* test, and the red (blue) denotes the positive (negative) SAT region above the 95% confidence level based on a two-sided Student's *t* test.

sensitive to the sample number of $NAO^-$ events. For NAO-unrelated UB events, the QB-WACE anomaly is still apparent but weaker than that for $NAO^+$-related UB events (Fig. 5c). The main cause of the strong QB-WACE anomaly for the $NAO^+$ pattern is that a strong UB anomaly can form under the $NAO^+$ condition (Fig. 5a), thus leading to strong arctic warming and continent cooling. This result is not sensitive to the sample number of $NAO^+$ events as seen in Fig. 6a.

For the 0.5-STD case (Fig. 6), a strong QB-WACE anomaly is still seen for $NAO^+$-related UB events in Fig. 6a compared to in Fig. 5a for a 1.0-STD case. This means the result that the QB-WACE anomaly is strong for $NAO^+$-related UB events is not sensitive to the sample number of $NAO^+$-related UB events. For $NAO^-$-related UB events (12 cases), the cold anomaly of the QB-WACE anomaly pattern, as seen in Fig. 6b, is evidently weaker than the case of $NAO^-$-related UB events with fewer number of samples, as in Fig. 5b. This means that the QB-WACE anomaly is influenced by the sample number of $NAO^-$-related UB events. The QB-WACE anomaly is also seen for UB events associated with $NAO^+$-to-$NAO^-$ transition events (Fig. 6c). Furthermore, we can see that the cold anomaly of the composite QB-WACE anomaly remains stronger for NAO-unrelated UB events (Fig. 6d), although this may be associated with its smaller sample size (five cases). If the number of NAO-unrelated UB events is significantly increased, the cold anomaly of the composite QB-WACE anomaly is not markedly weakened (Fig. 5c). This indicates that the composite QB-WACE anomaly is not strongly sensitive to the sample number of UB events without NAO. Even so, it appears that the $NAO^+$-related UB events turn out to be most favorable for the intense QB-WACE anomaly (Figs. 5a and 6a), while the QB-WACE anomaly can be seen in the presence of UB events without NAO and with $NAO^-$ events. The arctic warming and cold Eurasian winters take place simultaneously if a UB pattern occurs, but the phase of the NAO and its regime transition can modulate the QB-WACE anomaly in intensity and location, while the trend of the QB-WACE pattern comes from the sea ice loss over the BKS region itself, as noted in Part I. Because the frequency of NAO-related UB events is much lower for a 1.0-STD case than for a 0.5-STD case, our following classification of $NAO^+$-related UB events will be focused on the 0.5-STD case.

### c. *Impact of different positions of $NAO^+$-related UB events on the QB-WACE anomaly*

Motivated, in part, by the case study on an extreme cold event that occurred over southern China in January 2008, it is insightful to classify the 28 UB events with $NAO^+$ into northward- and southward-displaced (westward- and eastward-displaced) events by tracking the north–south (west–east) position of the anticyclonic center of the time-mean UB geopotential height anomaly averaged during its life cycle relative to the mean position of all UB events. Here, the mean latitude and longitude of the 28 $NAO^+$-related UB events are 63°N and 60°E, respectively. Then, the latitude (longitude) deviation of each event from the mean latitude (longitude) can be calculated. For the 28 $NAO^+$-related UB events, 10 (10) cases of the UB events are considered as northward (southward) displaced if the normalized latitude value of the UB event is greater (less) than the +0.5 (−0.5) standard deviation. Similarly, eight (seven) cases of the UB events are considered as eastward (westward) displaced if the normalized longitude value of the UB event is greater (less) than the +0.5 (−0.5) standard deviation. This is easily understood because the observed UB is not normally distributed in latitude and longitude.

The composite anomalies of time-mean 500-hPa geopotential height and SAT averaged from lag −5 to 5 days are shown in Figs. 7a–d for the northward-, southward-, westward-, and eastward-displaced UB events. It can be seen that for the northward-displaced UB events the composite geopotential height anomaly over the Ural region is relatively strong and exhibits a dipole structure that is located more northward, although the time-mean $NAO^+$ dipole anomaly over the Atlantic is relatively weak (Fig. 7). In fact, the weak time-mean $NAO^+$ anomaly does not mean that the $NAO^+$ events are weak. This is because the time-mean anomaly field in Fig. 7 is based on a time average from lag −5 to lag 5 around the UB peak (lag 0 day), which has an approximate 4–7-day lag behind the $NAO^+$ pattern. If a time average from lag −5 to lag +5 around the $NAO^+$ peak is used, then the resultant time-mean $NAO^+$ dipole anomaly is strong (see Fig. 14 below). Thus, we cannot conclude from Fig. 7 that the $NAO^+$ pattern associated with the UB is weak. On the other hand, we also see that the northward-displaced UB pattern (Fig. 7a) is about 8° north of the southward-displaced UB pattern (Fig. 7b), while there is a nearly 25° displacement for the eastward-displaced UB (Fig. 7c) relative to the westward-displaced UB (Fig. 7d). The variation of the UB location is statistically significant at the 95% confidence level for a Monte Carlo test. Thus, this indicates that the above classification of the UB location is useful for exploring the cause of the QB-WACE variability.

For a northward-displaced UB pattern, its combination with the $NAO^+$ dipole anomaly forms a quadrupole structure. The UB dipole anomaly leads to an intense QB-WACE anomaly pattern with a widespread cold anomaly from eastern Europe to Siberia and an arctic

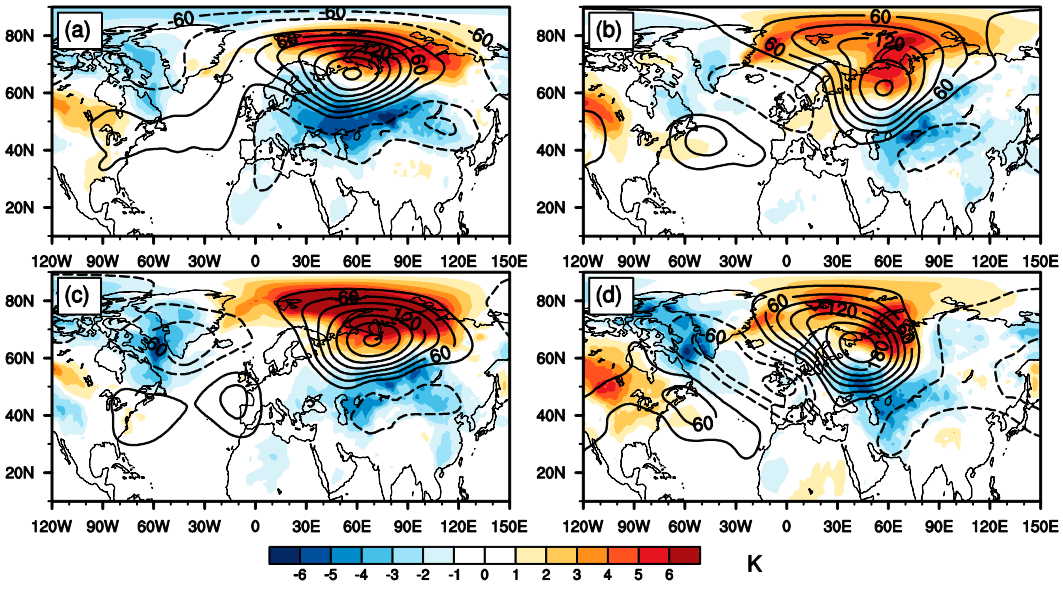


FIG. 7. Time-mean anomalies of 500-hPa geopotential height (gpm; contour interval = 30 gpm) and surface air temperature (K; colors) for $NAO^+$-related UB events during winters of 1979–2013 averaged from lag −5 to 5 days for (a) northward-, (b) southward-, (c) eastward-, and (d) westward-displaced $NAO^+$-related UB events. Lag 0 denotes the day at the peak of the UB event. In (a)–(d), the contours represent the region above the 95% confidence level based on a two-sided Student's *t* test, and the red (blue) denotes the positive (negative) temperature anomaly area above the 95% confidence level.

warm anomaly over the BKS region because the warm (cold) temperature advection takes place in the upstream (downstream) side of the blocking anticyclone (cyclone). The cold anomaly of the QB-WACE anomaly pattern is seen to reach northeastern China but not southern China, in that the SAT decline is confined to the north of 35°N (Fig. 7a). For southward-displaced UB events, the composite $NAO^+$ and UB height anomalies exhibit SW–NE- and SE–NW-oriented dipoles and they combine to form a low-frequency (~7–30 days) wave train (Fig. 7b), which resembles an $EA/WR^-$ pattern. Such a pattern is also seen for the eastward- and westward-displaced UB events (Figs. 7c,d). For southward- and eastward-displaced UB events, the cold SAT anomalies spread eastward to central Siberia and extend southward over East Asia to affect Mongolia and China, and even southern China (Figs. 7b,c). Thus, for southward- and eastward-displaced $NAO^+$-related UB events, persistent low temperatures over southern China are more likely to take place if the $NAO^+$ and UB events concur. For the westward-displaced UB events, the cold anomaly is concentrated in eastern Europe, central-western Siberia, Iran, Afghanistan, Pakistan, Mongolia, and northwestern China (Fig. 7d) and does not affect southern China. For this case, the cold anomaly is mainly located in central Asia. Thus, the QB-WACE anomaly is likely modulated by the strength and orientation of the $NAO^+$ dipole through the variation of the UB pattern.

## 5. The initiation of UB dipole anomalies and its possible link with $NAO^+$ events

In the above section, our investigation revealed that the QB-WACE anomaly is modulated by the $NAO^+$ variability through the UB variation. In this section, we quantify how the UB pattern is connected to upstream $NAO^+$ events. Furthermore, we explore whether the UB arises from the high-frequency eddy forcing over the Ural region or the propagation of low-frequency waves originating from the midlatitude North Atlantic. This is important for understanding the energy source of the UB pattern and what physical processes determine the initiation and intensification of UB dipole anomalies.

### *a. Spatial evolution of UB and $NAO^+$ dipole anomalies*

Figures 8–11 show the time evolution of the composite daily 500-hPa geopotential height anomalies for the northward-, southward-, eastward-, and westward-displaced UB events, respectively. Although the $NAO^+$ dipole anomalies in Figs. 8–11 are relatively weak, it does not mean that the UB is not associated with the $NAO^+$. In fact, the UB frequency is closely related to the $NAO^+$, as noted in Part I (their Fig. 16). The weak $NAO^+$ anomalies seen in Figs. 8–11 are easily explained, as the composite of daily height anomalies is centered on the UB peak. This leads to a result that the weak $NAO^+$

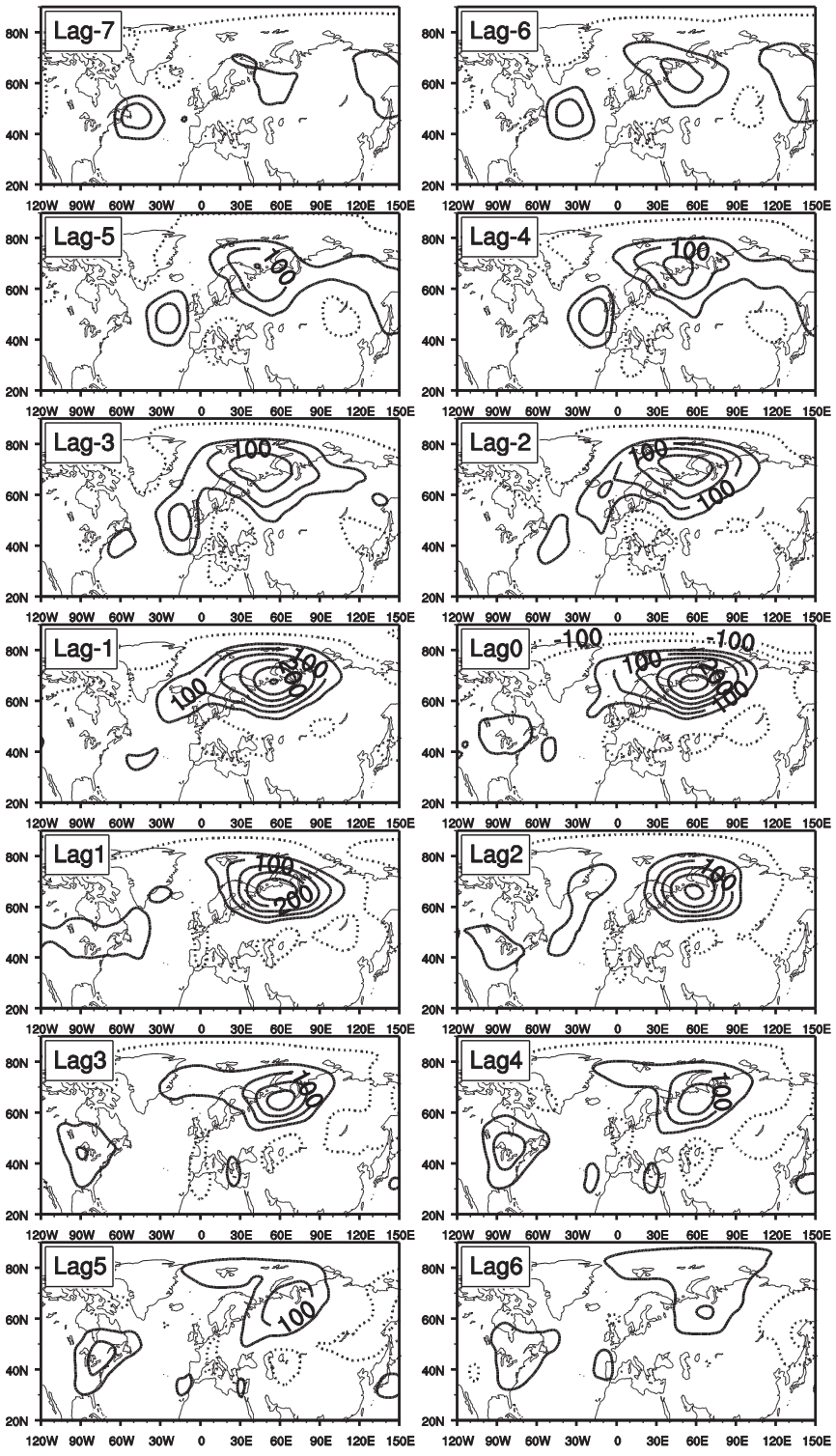


FIG. 8. Instantaneous fields of composite daily 500-hPa geopotential height anomalies (gpm; contour interval = 50 gpm) for 10 northward-displaced $NAO^+$-related UB events during the winters of 1979–2013 based on ERA-Interim. Lag 0 denotes the day of the UB amplitude peak, and only the contours for the regions above the 95% confidence level based on a two-sided Student's *t* test are plotted.

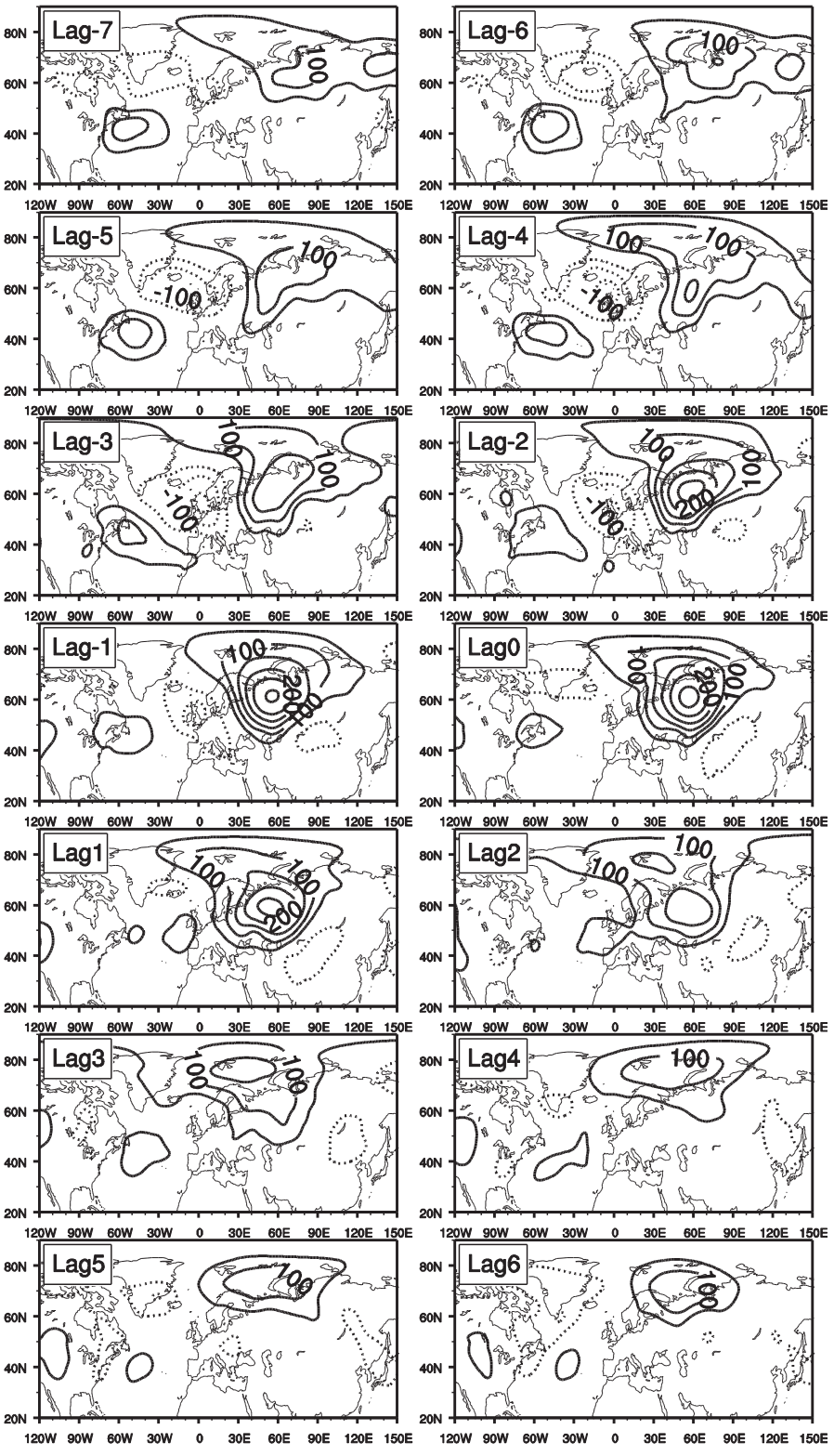


FIG. 9. As in Fig. 8, but for 10 southward-displaced $NAO^{+}$-related UB events.

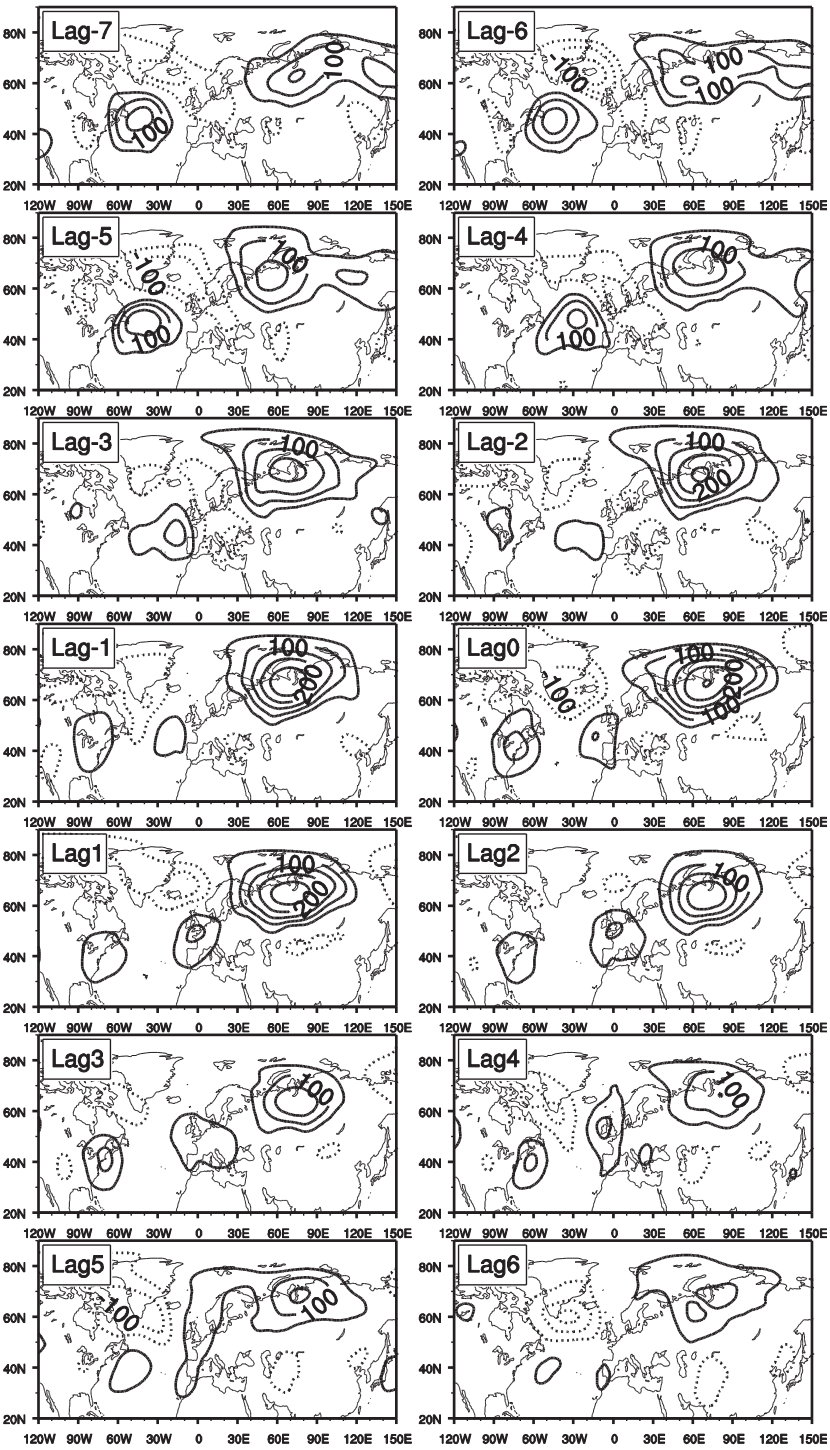


FIG. 10. As in Fig. 8, but for eight eastward-displaced $NAO^+$-related UB events.

anomalies at lag −7, −6, and −5 days are seen in Figs. 8–11 because each $NAO^+$ event may have different strength, location, and lifetime. However, if the peak of the $NAO^+$ index is chosen as a composite base (lag 0 day), then the composite daily NAO indices of $NAO^+$ events for northward-, southward-, eastward-, and westward-displaced UB events show that the $NAO^+$ event associated with the UB is strong (not shown). It can also be seen that for the northward-displaced UB events the decay of the $NAO^+$ dipole

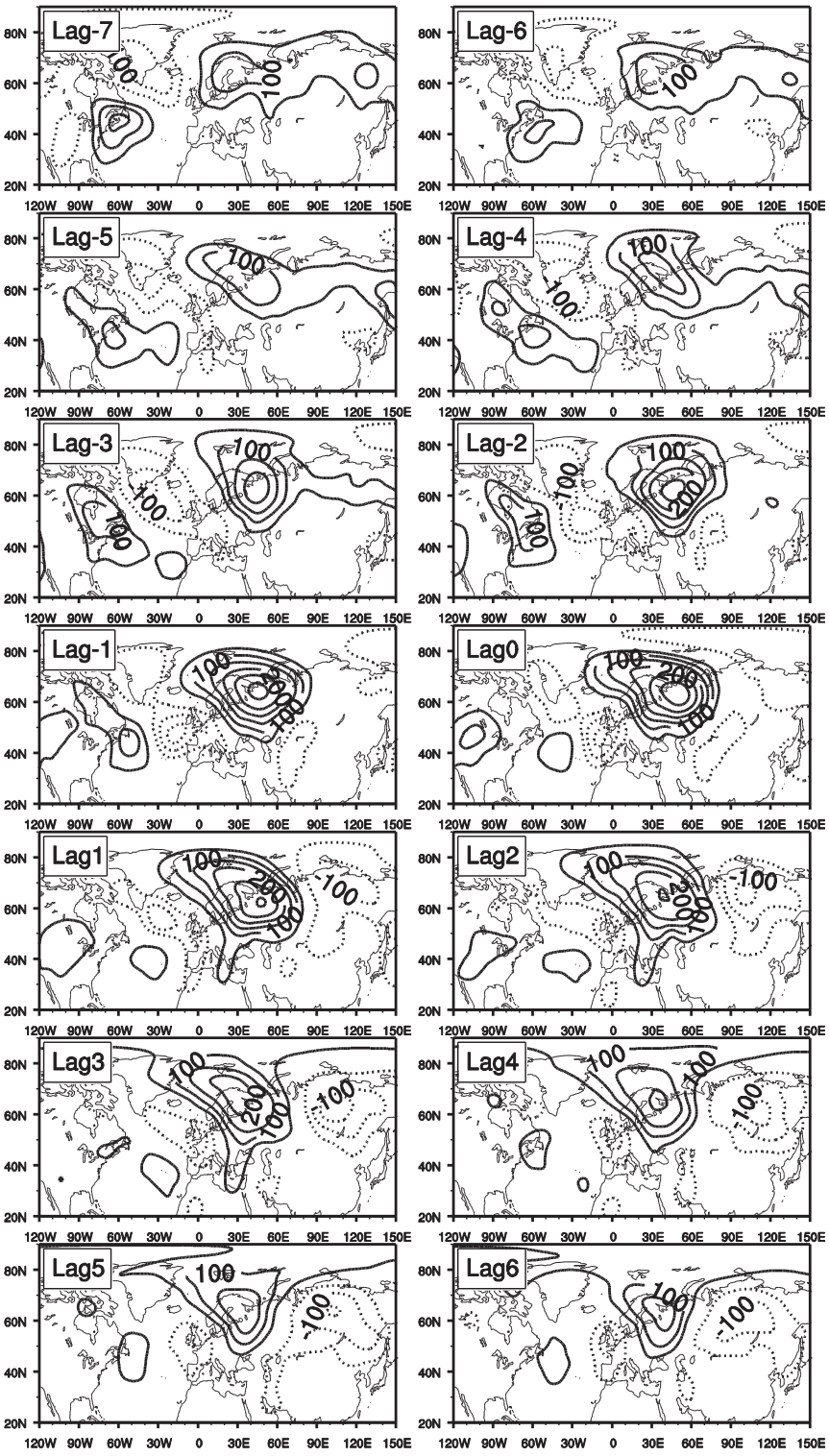


FIG. 11. As in Fig. 8, but for seven westward-displaced $NAO^+$-related UB events.

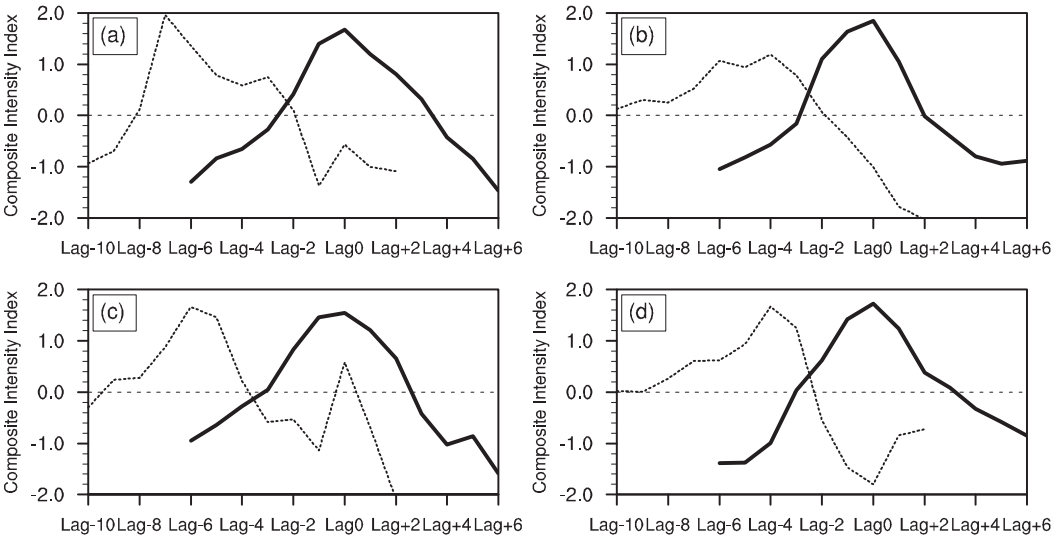


FIG. 12. Time evolutions of the normalized composite daily $NAO^+$ (dashed) and UB (solid) intensity indices for (a) northward-, (b) southward-, (c) eastward-, and (d) westward-displaced $NAO^+$-related UB events. Lag 0 denotes the day when the UB anomaly peaks. The $NAO^+$ intensity is defined as the difference of regionally averaged 500-hPa geopotential height anomaly between two regions (30°–50°N, 60°W–0° and 50°–70°N, 60°W–0°). The UB intensity is defined as the maximum amplitude value of the UB anticyclonic anomaly.

anomaly from lag −7 to 0 days is followed by the intensification of the composite UB anomaly (Fig. 8). According to the theoretical analysis of Luo et al. (2007, 2015b), the local amplification of an anticyclonic anomaly around 70°N and 60°E is a result of the accumulation of Rossby wave energy over the Ural region through the decay of the $NAO^+$ dipole anomaly (Fig. 12 of Luo et al. 2015b). For this case, the wave train structure of the $NAO^+$ and UB combined anomaly is less evident while it undergoes a slow eastward movement and gradually becomes one part of the anticyclonic circulation in the upstream side of the UB pattern (Fig. 8).

For the southward-displaced UB events, the UB anomaly originates from the intensification of a positive anomaly east of 60°E and moves slowly southwestward as it intensifies (Fig. 9 from lag −7 to 0 days). An interesting feature we find is that the intensifying $NAO^+$ dipole tends to tilt along the SW–NE direction so that its combination with the UB anticyclone anomaly results in a wave train structure similar to an $EA/WR^-$ pattern from the North Atlantic basin to the Eurasian continent. Thus, we conclude that the downstream propagation of a low-frequency (~7–30 days) wave train from the North Atlantic to the Ural region may reinforce and amplify southward-displaced UB anomalies. Such a process may also play an important role in the establishment of eastward- and westward-displaced UB events because they have similar spatial patterns (Figs. 10 and 11). To test this suggestion, it is also important to calculate the lead–lag relationship between $NAO^+$ and UB dipole anomalies, eddy-induced streamfunction tendency, and wave activity flux during the $NAO^+$ or UB life cycle. If the low-frequency eddy-induced streamfunction tendency is strong over the Ural region during the $NAO^+$ episode and if the low-frequency waves, as described by the wave activity flux vector, originate from the North Atlantic, incoming low-frequency waves from the North Atlantic to the Ural region are likely important for the excitation of UB anomalies. According to the investigation of Luo et al. (2007), there is inevitably a time lag of the UB pattern behind the $NAO^+$ pattern as the UB pattern arises from the energy dispersion of the $NAO^+$ event as a result of its decay (Luo et al. 2007, their Fig. 5). If the $NAO^+$ and UB patterns satisfy such a lead–lag relationship, the energy source of the UB is likely to come from the $NAO^+$ pattern over the North Atlantic. This lead–lag relationship can help us to identify how the UB pattern is connected to the $NAO^+$.

### b. *Lead–lag relationship between UB and $NAO^+$ events*

Because the daily NAO index cannot reflect the different location and variation of the $NAO^+$ and UB strengths, we need to redefine their intensity indices to describe the lead–lag relationship between $NAO^+$ and UB anomalies. In this subsection we define the maximum amplitude of the UB anticyclonic anomaly as the UB intensity and the difference of the regionally averaged 500-hPa geopotential height anomaly between the two regions 30°–50°N, 60°W–0° and 50°–70°N, 60°W–0° as

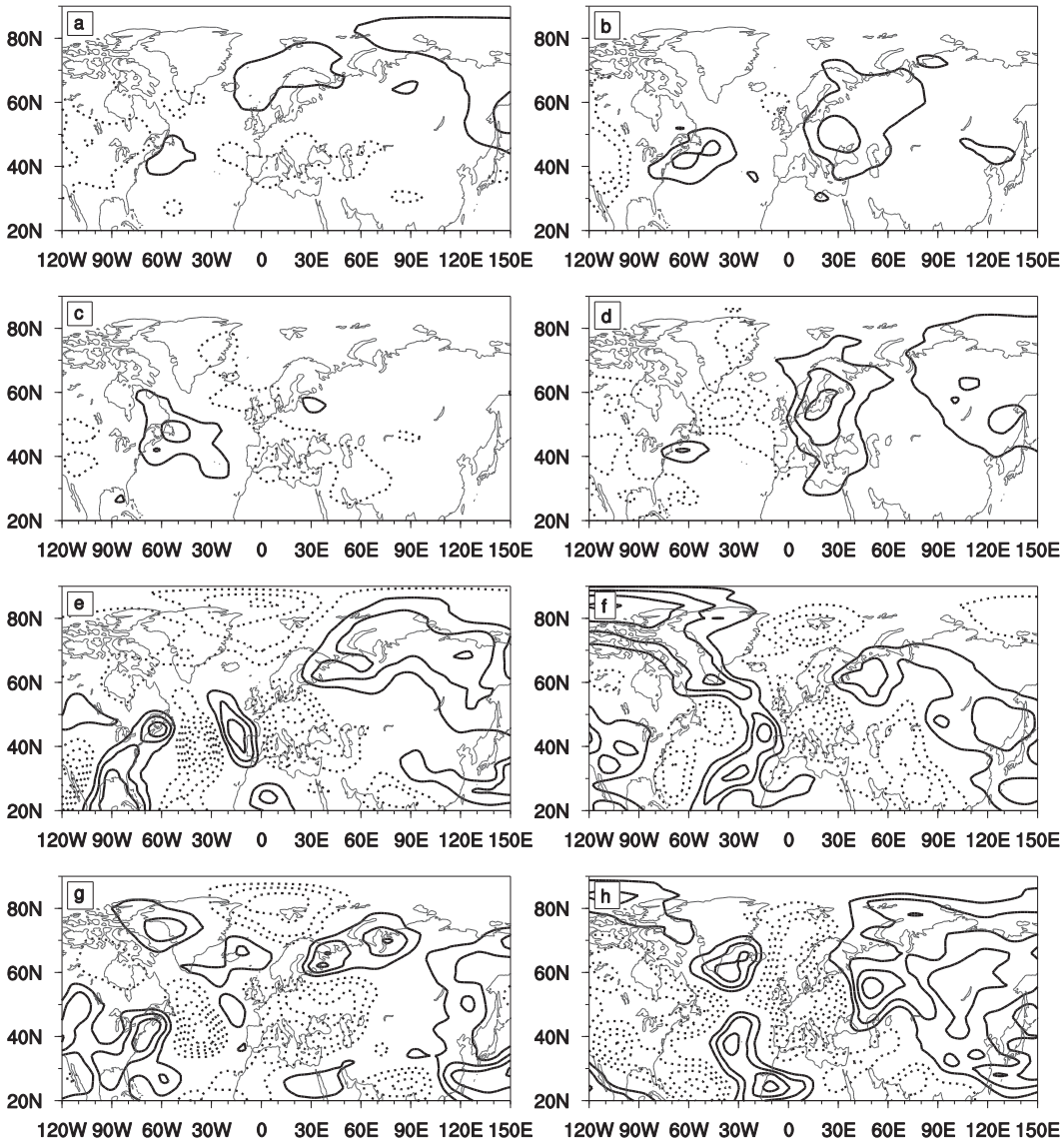


FIG. 13. Time-mean 250-hPa (a)–(d) high-frequency (2.5–6 days) and (e)–(h) low-frequency (~7–30 days) eddy-induced streamfunction tendency anomalies $\psi^{\text{vort}}$ ($\text{m}^2\,\text{s}^{-1}$; contour interval = $12\,\text{m}^2\,\text{s}^{-1}$, zero contour is omitted) averaged from lag −5 to 5 days for NAO$^+$-related UB events for (a),(e) northward-, (b),(f) southward-, (c),(g) eastward-, and (d),(h) westward-displaced UB events. Lag 0 denotes the day when the NAO$^+$ peaks. The solid (dashed) lines represent the anticyclonic (cyclonic) anomalies.

the NAO$^+$ intensity. Then, the normalized composite daily UB and NAO$^+$ intensity can be examined (Fig. 12) for northward- and southward-displaced (eastward- and westward-displaced) NAO$^+$-related UB events. For each of the four cases we shift the UB intensity index to determine the lag at which the strongest correlation is achieved. This yields correlations of 0.87, 0.74, 0.79, and 0.63 (all significant at the 95% confidence level) with the NAO$^+$ intensity index for the northward-, southward-, eastward-, and westward-displaced UB events that lag the NAO$^+$ intensity peak by 7, 4, 6, and 4 days, respectively. Thus, we find that UB events mainly originate from NAO$^+$ events through the energy accumulation of the NAO$^+$ anomaly toward the Ural region or the propagation of low-frequency wave trains related to the NAO$^+$ decay into the Ural region. This can also be verified by calculating the eddy-induced streamfunction tendency field and the wave activity flux vector. In particular, we find that low-frequency waves (eddies) are likely important for the excitation of subsequent UB anomalies if the low-frequency eddy-induced streamfunction tendency, $\psi^{\text{vort}} = \nabla^{-2}[-\nabla \cdot (\overline{\mathbf{v}'q'})]$, for low-pass-filtered eddies, as

defined in appendix A, is a large term compared to the high-frequency eddy-induced term (Hoskins et al. 1983; Nakamura et al. 1997) during the $NAO^+$ episode. To validate this finding, it is necessary to calculate the high- and low-frequency eddy-induced streamfunction tendency terms and compare their magnitudes, which is done in the next subsections.

### c. *Relative roles of high- and low-frequency eddies in UB anomalies*

As revealed above, the UB lags the $NAO^+$ by approximately 4–7 days. Thus, it is relevant to calculate eddy-induced streamfunction tendency anomaly $\psi^{vort}$ fields of high- and low-pass-filtered eddies to estimate the relative roles of high- and low-frequency eddies in the establishment of subsequent UB events during the $NAO^+$ life cycles.

Figure 13 shows the 250-hPa high- (~2.5–6 days) and low-frequency (~7–30 days) transient eddy-induced streamfunction tendency anomaly $\psi^{vort}$ field averaged over the period from lag −5 to 5 days around the $NAO^+$ peak (lag 0 day) for all the northward-, southward-, eastward-, and westward-displaced UB events during the winters of 1979–2013. It is seen that during the $NAO^+$ period the high-frequency eddy-induced vorticity forcing $\psi^{vort}$ is extremely weak over the Ural region, while it shows large positive values over the European continent for southward- and westward-displaced UB events (Figs. 13b,d). This suggests that high-frequency eddies may not be particularly important for the establishment of UB events, while they are important for the NAO and some of the European blocking and UB events.

On the other hand, we can see that the large-value regions of the high-frequency eddy-induced $\psi^{vort}$ anomaly field are mainly concentrated in the North Atlantic basin for the four types of the UB events (Figs. 13a–d). The regions of large values correspond closely to those with strong winter cyclone and frontal activity (Simmonds and Keay 2002; Rudeva and Simmonds 2015). This implies that high-frequency (synoptic scale) eddies seem to play a more important role in the establishment of the $NAO^+$ pattern than in the UB formation. The low-frequency eddy-induced $\psi^{vort}$ anomaly field shows large values over the North Atlantic and Europe and especially has large positive values over the Ural Mountains and its adjacent regions for all the types of UB events (Figs. 13e–h), thus indicating that during the $NAO^+$ episode low-frequency waves are rather active in the region from the North Atlantic to Eurasian continent and possibly contribute to the UB establishment. This result is acceptable only during the mature phase of the NAO flow because it can be approximately considered as a time-mean flow, while the NAO is essentially a low-frequency wave. For further discussion, refer to appendix A. Although this result is less strict, it can be further justified by calculating the wave activity flux vector as in Takaya and Nakamura (2001). While the high-frequency eddies drive the NAO event, the decay of an $NAO^+$ event can excite subsequent downstream blocking due to its energy dispersion (Luo et al. 2007). This may explain why the UB events always lag the $NAO^+$ events, as noted above (Fig. 12). As we will reveal by calculating the wave activity flux vectors, the propagation of upstream low-frequency (~7–30 days) waves into the Ural region is crucial for the UB establishment. This method has also been used by Nakamura et al. (1997), who demonstrated that a quasi-stationary wave train across the North Atlantic can contribute to the blocking amplification over Europe and Siberia. In the next subsection, we will demonstrate that the generation of UB anomalies comes mainly from the propagation of low-frequency wave trains generated in the midlatitude North Atlantic, at least for southward-, eastward-, and westward-displaced UB anomalies.

### d. *Do the UB anomalies originate from the propagation of low-frequency wave trains associated with $NAO^+$ events?*

To establish whether the low-frequency wave trains emanate from the midlatitude North Atlantic, it is useful to calculate the time-mean horizontal wave activity flux vector $\mathbf{W}_h$ defined by Takaya and Nakamura (2001), as described in appendix B, during the $NAO^+$ episodes (from lag −5 to +5 days from the $NAO^+$ peak) for northward-, southward-, eastward-, and westward-displaced UB events. Because the UB peak lags the $NAO^+$ peak by 4–7 days (depending on which of the four cases is considered), the time-mean $\mathbf{W}_h$ can reflect the contribution of low-frequency wave propagation to the UB amplification. Thus, it is reasonable to only present the time-mean wave activity flux vector in Fig. 14, which shows that low-frequency wave trains are less evident for northward-displaced UB events (Fig. 14a). This indicates that the northward-displaced UB events may result from the direct energy dispersion of the $NAO^+$ pattern rather than from the propagation of low-frequency wave trains formed by the decay of the $NAO^+$ pattern. The physical explanation of this result will be provided below. For southward-, eastward-, and westward-displaced UB events [which account for 64% (18 of 28 cases) of all the displaced UB events], the large $\mathbf{W}_h$ vectors point to the northeast direction from the midlatitude North Atlantic to northern Europe and then turn to the southeast from the Ural region to East Asia (Figs. 14b–d), thus indicating that these UB events originate from the propagation of the low-frequency wave trains from the midlatitude North Atlantic to the Ural region. However,

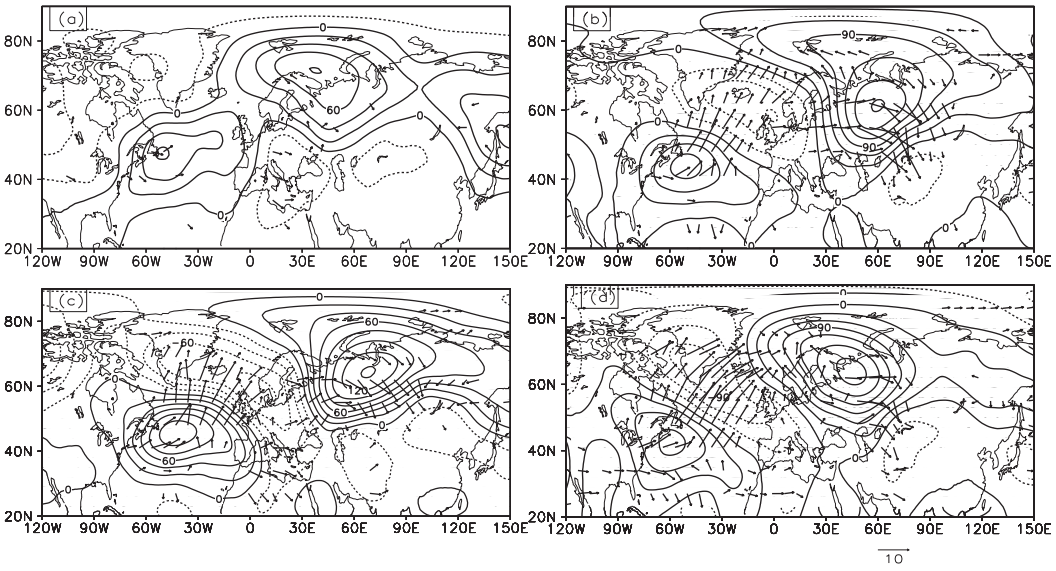


FIG. 14. Time-mean horizontal wave activity flux $\mathbf{W}_h$ ($m^2\ s^{-2}$; arrows) and 500-hPa geopotential height anomalies (gpm; contour interval = 20 gpm) of low-frequency eddies with time scales from 7 to 30 days averaged from lag −5 to 5 days for (a) northward-, (b) southward-, (c) eastward-, and (d) westward-displaced $NAO^+$-related UB events, where lag 0 denotes the day when the $NAO^+$ peaks. The solid (dashed) lines represent positive (negative) height anomalies.

we note that this structure is not apparent for the northward-displaced UB events (Fig. 14a).

In summary, the propagation of low-frequency wave trains generated in the midlatitude North Atlantic can modulate the QB-WACE pattern through the generation and variation of UB events. However, what factors determine the spatial structure of the $NAO^+$ and UB combined anomalies and the location of UB anomalies will be explored in the next section.

## 6. Factors affecting the wave train structure of the $NAO^+$ and UB combined anomalies and the location of UB

As indicated above, because the UB events lag the $NAO^+$ events by 4–7 days (Fig. 13), the time-mean zonal wind associated with an $NAO^+$ event averaged from lag −5 to 5 days from the $NAO^+$ peak may be considered as the background condition for the UB event. The 10-day time-mean composite 500-hPa zonal wind anomalies are shown in Figs. 15a–d for the northward-, southward-, eastward-, and westward-displaced UB events, while the meridional profiles of the corresponding time- and zonal-mean zonal wind averaged from lag −5 to 5 days and over 60°W–0° are plotted in Figs. 15e,f.

It can be seen that because the zonal wind in the North Atlantic basin is almost uniform in the meridional direction (dashed line in Fig. 15e) and its anomaly is relatively weak (Fig. 15a) for the northward-displaced case, the 500-hPa geopotential height anomaly from the North Atlantic to the Eurasian continent does not exhibit a low-frequency wave train–like pattern (Fig. 14a) (consistent with what we found above), although the $NAO^+$ dipole anomaly can decay from lag −7 to 0 days in Fig. 8. However, for the southward-, westward-, and eastward-displaced UB events, the positive zonal wind anomaly (Figs. 15b–d) or the jet (solid line in Fig. 15e and solid and dashed lines in Fig. 15f) over the North Atlantic is relatively strong so that a quasi-stationary wave train resembling the EA/$WR^-$ pattern can easily be seen (Figs. 14b–d). This is because the strong asymmetric jet can lead to the spatial tilting of a dipole anomaly so as to excite a wave train structure (Luo et al. 2010). Of course, the strong North Atlantic jets are also seen to be acting as waveguides for the quasi-stationary wave train (Hoskins and Ambrizzi 1993). Thus, the strength of the North Atlantic jet is an important factor that determines whether an EA/$WR^-$ pattern is generated when the $NAO^+$ and UB anomalies coexist. The numerical experiment of Luo et al. (2010) indicates that the wave train structure cannot be formed when the mean westerly wind is uniform or exhibits a symmetric jetlike distribution, even though the $NAO^+$ dipole anomaly spreads its energy downstream (Fig. 8). This is the case for the northward-displaced $NAO^+$-related UB patterns (Fig. 14a and dashed line in Fig. 15e). Thus, when the North Atlantic jet is strong, as seen for southward-, eastward-, and westward-displaced UB events, the $NAO^+$ anomaly can favor the UB because of its energy dispersion through the wave train propagation

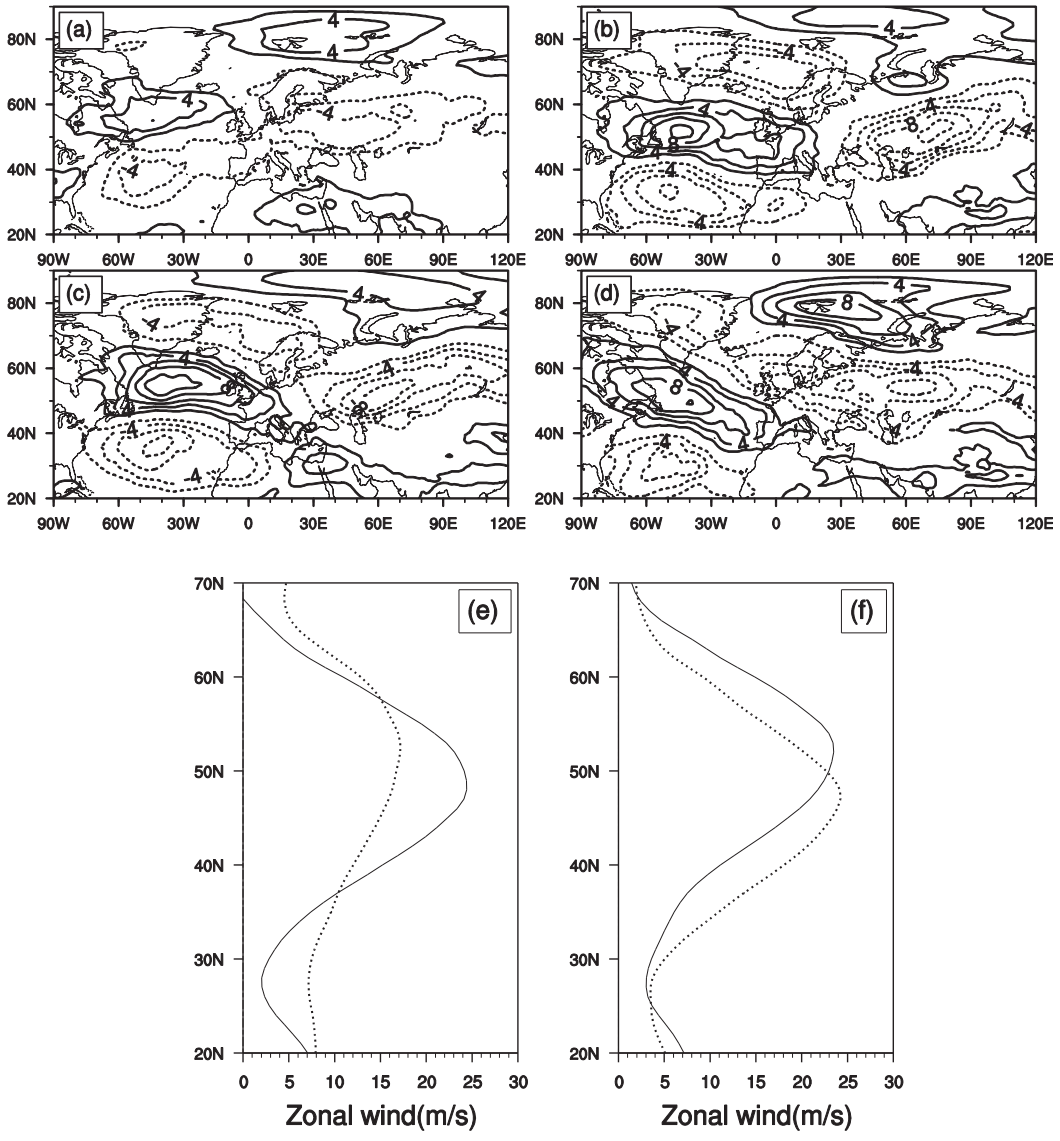


FIG. 15. Time-mean 500-hPa zonal wind anomalies ($m\,s^{-1}$; contour interval = $2\,m\,s^{-1}$) from lag −5 to 5 days during the $NAO^+$ episodes for (a) northward-, (b) southward-, (c) eastward-, and (d) westward-displaced UB events, where lag 0 denotes the day when the $NAO^+$ amplitude peaks. The contours are plotted for the region above the 95% confidence level based on a two-sided Student's *t* test. Also shown are the latitudinal profiles of the zonally averaged 500-hPa zonal wind from lag −5 to 5 days over the region 60°W–0°, where the solid (dashed) lines denote the cases for (e) southward- (northward-) and (f) eastward- (westward-) displaced UB events.

like an $EA/WR^-$ pattern (Figs. 9–11). When the North Atlantic jet is relatively weak, the $NAO^+$ anomaly can strengthen the UB through its energy dispersion but in a form unlike an $EA/WR^-$ pattern (Fig. 8).

Figures 15a–d also show that the zonal wind anomalies exhibit positive–negative–positive tripole patterns from the higher-to-lower latitudes over the Eurasian continent. The location of the weak zonal wind over Eurasia (i.e., the negative wind anomaly of Fig. 15) may roughly correspond to the occurrence region of subsequent blocking events. In Fig. 15a, a relatively weak zonal wind anomaly emerges in the region from 40° to 70°N and from 20° to 90°E, thus favoring the occurrence of UB events in higher-latitude regions. This corresponds to the case of northward-displaced UB events (Fig. 7a). Prior to the southward-displaced UB onset, the large negative zonal wind anomalies, which would weaken the zonal westerly wind, appear in a region centered near 45°N and 70°E (Fig. 15b). Such a weakened westerly wind is favorable for subsequent UB events over the southern Ural region

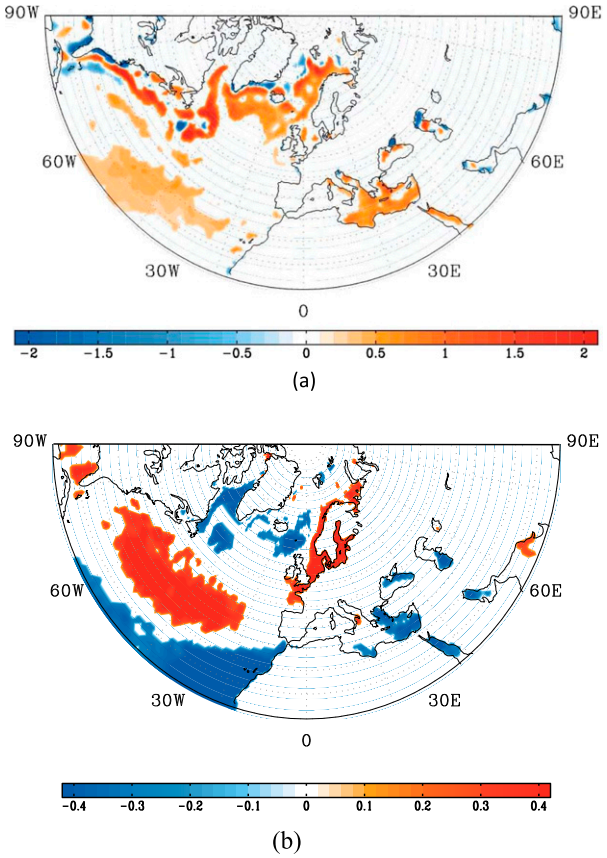


FIG. 16. (a) The P2 minus P1 difference of the DJF-mean sea surface temperature (°C), in which only the regions above the 95% confidence level are shaded and (b) spatial correlation coefficients of the detrended DJF-mean SST anomalies with the NAO indices, in which only regions above the 90% confidence level are shaded.

(Fig. 7b) because its negative westerly wind anomaly is located more southward than for the northward-displaced UB. Figures 15c,d further show that prior to the eastward- and westward-displaced UB events the negative zonal wind anomalies are seen in the region from 40° to 120°E and from 10°W to 80°E, respectively. The regions of the negative zonal wind anomalies should correspond to the occurrence locations of subsequent UB events (Figs. 7c, d). On the other hand, because the positive zonal wind anomalies (Fig. 15c) extend to the European continent, they suppress the retrogression of the UB pattern and thus favor eastward-displaced UB events. However, it is difficult for this case (i.e., Fig. 15c) to happen for the westward-displaced UB in Fig. 15d. Thus, the location of the UB events seems to be dominated by the areas with weak zonal wind over Eurasia and the eastward or westward extension of the strong westerly jet (positive zonal wind anomaly) over the North Atlantic. For the southward-displaced UB, the positive westerly anomaly over the North Atlantic also extends eastward (Fig. 15b). In other words, the eastward- and southward-displaced UB events tend to occur when the North Atlantic jet is strong and has an eastward extension. As noted in Part I, the weakening of zonal winds over the Eurasian continent is related to the arctic warming associated with the sea ice loss over the BKS. Although many previous studies mentioned this point (Newson 1973; Comiso et al. 2008; Screen and Simmonds 2010; Hori et al. 2011; Overland et al. 2011; Inoue et al. 2012; Mori et al. 2014; Walsh 2014), the different existing regions of the weak westerly wind related to the BKS sea ice loss that determines the different occurrence regions of the UB were not noted. Thus, in this section two important conclusions are reached: 1) the strength and asymmetry of the North Atlantic jet determine whether the $NAO^+$ can form an $EA/WR^-$ pattern wave train, and 2) the region of weak zonal wind over Eurasia and the zonal extent of the strong North Atlantic jet dominate the location of UB events. As has been demonstrated in Luo et al. (2015a,b), during an $NAO^+$ episode, blocking tends to occur over the downstream side of the European continent when the North Atlantic jet (storm track) is strong (weak). Thus, the UB is also likely influenced by the North Atlantic warming through changes in the North Atlantic jet and storm track.

Although this paper is focused on examining how the $NAO^+$ and North Atlantic conditions modulate the UB variability and associated QB-WACE variation, it is also useful to look at how the surface sea temperature (SST) in the North Atlantic basin varies from P1 to P2 and the correlation of the NAO index with the detrended SST anomaly because the $NAO^+$ pattern often corresponds to a long-lived UB. In Fig. 16a we see that the North Atlantic exhibits a more intense basin-scale warming during P2 compared to P1, except for the cooling over a small portion of the basin. The most evident warming is found over the BKS, North Atlantic high latitudes from the Labrador Sea to the southeast of Greenland, and the Gulf Stream region. The midlatitude North Atlantic warming is also evident. The basin-scale warming can crudely be explained by the decadal and multidecadal variations of the SST anomalies superimposed on a global warming trend (Walsh 2014). In particular, the strong positive SST anomalies south of the Gulf Stream extension (GSE) almost disappear when the SST is detrended (not shown). Thus, we conclude that it can be attributed to the decadal variations of the SSTs (Peings and Magnusdottir 2014, their Fig. 1a). Because the strong positive SST anomalies over the BKS are able to induce the weakening of middle-to-high-latitude westerly winds over Eurasia through warming the atmosphere over the BKS and its southern side, the variability of the SST anomaly or sea ice over the BKS probably may lead

to the variation of the existing region of weak westerly winds over Eurasia.

The correlation map of the detrended NAO index with SST anomalies over the North Atlantic basin is shown in Fig. 16b. It is seen that the NAO index exhibits a positive correlation with the SST anomalies over two regions—the BKS and midlatitude North Atlantic south of the GSE—but a negative correlation with the SST anomalies over the high-latitude North Atlantic north of the GSE. Thus, the positive SST anomalies over the midlatitude North Atlantic south of the GSE correspond to an $NAO^+$-like pattern, while the high-latitude positive SST anomalies north of the GSE that are associated with the sea ice loss over the NAH region correspond to an $NAO^-$-like pattern. This suggests that the midlatitude North Atlantic warming generates an $NAO^+$-like pattern (Czaja and Frankignoul 2002) and favors the long-lived UB pattern through the reduction of middle-to-high-latitude westerlies over Eurasia because of the BKS warming during P2 (see Fig. 16 in Part I). Conversely, the presence of the long-lived UB can further amplify the warming over the BKS region through the generation of a QB-WACE dipole anomaly. Thus, we conclude that SST variability over the North Atlantic likely causes changes in the $NAO^+$ pattern and North Atlantic jet, which in turn affect the UB and then the winter-mean WACE by altering the QB-WACE anomalies. These issues warrant further examination using numerical experiments and observational reanalysis.

## 7. Conclusions and discussion

We have examined the physical cause of UB variability and how such variability affects the QB-WACE pattern. We have classified UB patterns based on their zonal and meridional positions, motivated by a case study of a cold event that occurred over southern China in January 2008. The analysis of this cold event revealed that two UB events occurred from 31 December 2007 to 11 January 2008 (event 1) and from 15 to 31 January 2008 (event 2) and are associated with two $NAO^+$ events. Because the location of the UB pattern is distinctly different between event 1 and event 2, the large change in the UB location leads to the marked variability of the QB-WACE pattern. Thus, this motivates us to classify the UB pattern in terms of the location difference of the UB patterns.

A composite study of UB events during winters of 1979–2013 shows that for the 0.5 standard deviation (STD) definition of NAO events, the QB-WACE anomaly is more intense and evident for $NAO^+$-related UB events than other types of UB events. This conclusion also holds for a 1.0-STD definition of NAO events. In this paper, we classify only the $NAO^+$-related UB events because they are much more frequent than other types of UB events. For $NAO^+$-related UB events, the UB pattern is classified into northward- and southward-displaced (eastward- and westward-displaced) types by considering the latitudinal (longitudinal) location of the UB anticyclonic anomaly center. For the four types of the $NAO^+$-related UB events, the UB anomalies lag the $NAO^+$ dipoles by 4–7 days. This indicates that the decay of the $NAO^+$ dipole more likely leads to the initiation and amplification of the UB anomaly. Thus, the time lag of the UB behind an $NAO^+$ event implies a potential for predicting the QB-WACE anomaly or Eurasian cold events using the $NAO^+$ event approximately 4–7 days ahead. Besides northward-displaced events, the UB anomalies associated with other $NAO^+$-related UB events arise primarily from the propagation of a low-frequency (7–30 days) wave train resembling an $EA/WR^-$ pattern from the midlatitude North Atlantic into the Ural region across Europe through the decay and tilting of the $NAO^+$ dipole because of the role of a strong North Atlantic jet. For northward-displaced UB events the $EA/WR^-$ pattern produced by the UB and $NAO^+$ combined dipole anomalies is less evident because of a weak North Atlantic jet. Instead, the establishment of the northward-displaced UB pattern results mainly from the direct energy dispersion of the $NAO^+$ dipole anomaly rather than from the wave train propagation, which has been demonstrated by interpreting the eddy-induced streamfunction tendency and the horizontal wave activity flux vector.

For northward-displaced UB events, cold anomalies over Eurasia are mainly confined to relatively high-latitude regions, while the southward- and eastward-displaced $NAO^+$-related UB anomalies lead to eastward- and southward-displaced Eurasian cold anomalies with intrusion into southern China. In this paper we also found that the QB-WACE anomaly is modulated not only by the UB location and persistence but also by the strength of the North Atlantic jet through which a quasi-stationary wave train–like an $EA/WR^-$ pattern can be excited. The location of the UB anomaly is found to be collocated with the zonal extent of the North Atlantic jet and the existing region of weak zonal winds (negative zonal wind anomalies) over the Eurasian continent prior to the UB onset, which is more likely to be related to the arctic warming over the BKS region, as noted in Part I. Thus, the UB variability depends not only on the change in the existing region of weak westerly winds over Eurasia possibly due to the variation of arctic warming over the BKS but also the $NAO^+$ and North Atlantic conditions associated with the SST variability over the North Atlantic.

Finally, we calculated the P2 − P1 difference of SST anomalies between P2 and P1 and the correlation of the

winter-mean NAO index with the detrended SST anomaly. It is found that the North Atlantic Ocean undergoes a more marked basin-scale warming during P2 than P1. The distinct warming takes place mainly over the high-latitude and midlatitude North Atlantic, the Gulf Stream region, and the BKS. This suggests that the variability of the positive SST anomalies over the BKS and midlatitude North Atlantic may change the existing region of weak middle-to-high-latitude westerly winds over Eurasia and the zonal extent of the North Atlantic jet to induce the variation of the location of the long-lived UB event. On the other hand, the NAO index is seen to exhibit a positive (negative) correlation with the midlatitude (high latitude) North Atlantic SST anomaly, indicating that midlatitude North Atlantic warming tends to excite the $NAO^+$ event and then favor the UB pattern, while the high-latitude North Atlantic warming is favorable for the $NAO^-$. Our results also suggest that the variability of the SST anomalies over the North Atlantic is important for the variations of the $NAO^+$ pattern and associated North Atlantic jet that affect the UB and associated QB-WACE anomalies. This research has revealed many new findings as to the influences that give rise to the winter-mean WACE pattern and its variability. It has also raised many new questions, which can be explored with carefully designed numerical model experiments. These will be the focus of future studies.

*Acknowledgments.* The authors acknowledge the support from the National Science Foundation of China (Grants 41375067 and 41430533) and the National Basic Research Program of China (2015CB953903). A. Dai is supported by the U.S. National Science Foundation (Grant AGS-1353740), the U.S. Department of Energy's Office of Science (Award DE-SC0012602), and the U.S. National Oceanic and Atmospheric Administration (Award NA15OAR4310086). C. Franzke was supported by the German Research Foundation (DFG) through the cluster of excellence CliSAP (EXC 177) at the University of Hamburg. I. Simmonds is supported by Australian Research Council Grant DP 160101997. The authors thank three anonymous reviewers and Prof. Walsh, whose comments improved this paper, and Dr. Y. Yao, who plotted Fig. 16.

## APPENDIX A

### Eddy-Induced Streamfunction Tendency Method

In this paper, we used the eddy-induced streamfunction tendency method (Holopainen et al. 1982; Hoskins et al. 1983; Lau and Holopainen 1984; Holopainen and Fortelius 1987; Nakamura et al. 1997) to evaluate the role of high-pass (2.5–6 days) filtered (identified with Lanczos filters) transient eddies in the UB establishment during the $NAO^+$ period. In the eddy–mean flow interaction equation of Hoskins et al. (1983), the large-scale flow is assumed to be a time-mean flow.

If the atmospheric streamfunction is decomposed into a time-mean flow part $\overline{\psi}$ (time-mean streamfunction) and transient eddy part $\psi'$ (eddy streamfunction), then the quasigeostrophic barotropic eddy–mean flow interaction equation with an eddy-induced streamfunction tendency term can be expressed as follows (Hoskins et al. 1983):

$$\frac{\partial \overline{q}}{\partial t} + J(\overline{\psi}, \overline{q} + f) + f\nabla \cdot \overline{\mathbf{V}} = -\nabla \cdot (\overline{\mathbf{v}'q'}) - \mathbf{k} \cdot \nabla \times \mathbf{F}, \tag{A1}$$

where $\overline{q} = \nabla^2 \overline{\psi}$ is the relative vorticity of the time-mean flow, $f$ is the Coriolis parameter, $\nabla \cdot \overline{\mathbf{V}}$ is the divergence of the time-mean flow wind $\overline{\mathbf{V}}$, $\mathbf{v}' = (-\partial\psi'/\partial y, \partial\psi'/\partial x)$ is the wind vector of transient eddies and its relative vorticity $q' = \partial v'/\partial x - \partial u'/\partial y = \nabla^2\psi'$, $\mathbf{k}$ is the unit vertical vector, $\mathbf{F}$ is the frictional force, and overbars denote a time mean.

Analogous to Holopainen and Fortelius (1987), in a quasigeostrophic barotropic framework the effect of transient eddies on the time-mean flow in Eq. (A1) can be described by the eddy-induced streamfunction tendency in terms of the eddy vorticity flux of the relative vorticity as $(\partial\overline{q}/\partial t)_{\mathrm{TE}} = -\nabla \cdot (\overline{\mathbf{v}'q'}) = -\nabla \cdot \mathbf{D}_e$ and $\mathbf{D}_e = (D_{ex}, D_{ey}) = (\overline{u'q'}, \overline{v'q'}) = (-\mathbf{k} \cdot \nabla \times \mathbf{E}_m, \nabla \cdot \mathbf{E}_m)$, where $\mathbf{E}_m = [(\overline{v'^2} - \overline{u'^2})/2, -\overline{u'v'}]$. It should be pointed out that $-\mathbf{k} \cdot \nabla \times \mathbf{E}_m$ and $\nabla \cdot \mathbf{E}_m$ in the $\mathbf{D}_e$ vector are the vorticity and divergence of the $\mathbf{E}_m$ vector, respectively. Here, the $\nabla \cdot \mathbf{D}_e > 0$ ($\nabla \cdot \mathbf{D}_e < 0$) corresponds to an anticyclonic (cyclonic) forcing. To examine the contribution of transient eddies to the time-mean flow, it is useful to introduce a time-mean eddy-induced streamfunction tendency $\psi^{\mathrm{vort}}$ so that $\nabla^2\psi^{\mathrm{vort}} = -\nabla \cdot (\overline{\mathbf{v}'q'}) = -\nabla \cdot \mathbf{D}_e$ or $\psi^{\mathrm{vort}} = \nabla^{-2}(-\nabla \cdot \mathbf{D}_e)$ (Holopainen et al. 1982; Hoskins et al. 1983; Holopainen and Fortelius 1987). By calculating the $\psi^{\mathrm{vort}}$ field, one may evaluate the net contribution of transient eddies to the time-mean flow (Holopainen and Fortelius 1987; Nakamura et al. 1997). In our calculation, the climatological-mean $\mathbf{D}_e$ vector field and associated $\psi^{\mathrm{vort}}$ during the period 1979–2013 are removed to emphasize the variations of their anomaly parts $\psi_a^{\mathrm{vort}} = \nabla^{-2}(-\nabla \cdot \mathbf{D}_{\mathrm{ea}})$ and $\mathbf{D}_{\mathrm{ea}}$ associated with large-scale circulations ($\mathbf{D}_{\mathrm{ea}} = \mathbf{D}_e - \overline{\mathbf{D}}_e$, where $\overline{\mathbf{D}}_e$ is a DJF-mean vector field averaged during 1979–2013). Such $\psi_a^{\mathrm{vort}}$ and $\mathbf{D}_{\mathrm{ea}}$ fields are referred to as $\psi^{\mathrm{vort}}$ and $\mathbf{D}_e$ anomaly fields, hereafter.

Equation (A1) is relevant for diagnosing the role of high-pass-filtered eddies in the blocking (Hoskins et al. 1983) and NAO (Lau 1988) maintenance because the blocking and NAO flows can be crudely considered as time-mean flows. Hoskins et al. (1983) also applied it to diagnose the role of low-frequency transients in the blocking flow by assuming that the blocking is a time-mean flow. Obviously, such a treatment is less exact and problematic for low-pass-filtered eddies because the blocking itself is essentially a type of low-frequency eddy. However, this treatment is acceptable only when it is applied to the $NAO^+$ mature phase, because the $NAO^+$ may be crudely assumed to be time independent and because the $NAO^+$ and UB have an approximate 4–7-day time lag difference and appear over different zonal regions. Thus, we can conclude from the $\psi^{vort}$ anomaly distribution whether low-frequency eddies related to the $NAO^+$ contribute to the UB establishment by inspecting if the $\psi^{vort}$ anomaly averaged during the $NAO^+$ mature period has large or small positive values over the Ural region. In our calculation the time mean averaged from lag −5 to 5 days around the $NAO^+$ peak is approximately considered as the mature phase of the $NAO^+$.

## APPENDIX B

### Three-Dimensional Wave Activity Flux Vector

Because the eddy–mean flow interaction equation in Eq. (A1) is not exact for low-frequency eddies, it is necessary to use the time-mean horizontal wave activity vector $\mathbf{W}_h$ to diagnose the contribution of low-frequency eddies to the UB. Such a calculation can help us better understand whether the $NAO^+$ leads to a UB through the propagation of low-frequency wave trains emanating from the North Atlantic. In this paper, we use the three-dimensional wave activity fluxes in a nonuniform basic flow presented by Takaya and Nakamura (2001) to diagnose the propagation of a low-frequency wave train during the $NAO^+$ periods. The direction of the $\mathbf{W}_h$ vector indicates the energy propagation direction of low-frequency waves and where the wave energy comes from. A converging wave activity flux associated with an incoming quasi-stationary Rossby wave train is of primary importance in the UB formation. As shown in Fig. 12, because the UB peak lags the $NAO^+$ peak by approximately 4–7 days for different locations of UB events, the time mean of the wave activity flux vector $\mathbf{W}_h$ averaged over 10 days (from lag −5 to 5 days) centered on the $NAO^+$ peak (lag 0) can reflect the contribution of low-frequency wave propagation to the UB amplification during the $NAO^+$ period (growth and decay). For example, if the $\mathbf{W}_h$ vector originates from the North Atlantic, the propagation of low-frequency waves generated in the North Atlantic into the Ural region may be considered as a precursor or driving factor of the UB onset. The mathematical expression of $\mathbf{W}_h$ can be found in Takaya and Nakamura (2001). The climatological-mean wind in winter during 1979–2013 is considered as the basic wind field used to calculate $\mathbf{W}_h$. This result is not sensitive to the different choice of basic wind fields (not shown).

## REFERENCES


Barnston, A. G., and R. E. Livezey, 1987: Classification, seasonality and persistence of low-frequency atmospheric circulation patterns. *Mon. Wea. Rev.*, **115**, 1083–1126, doi:10.1175/1520-0493(1987)115<1083:CSAPOL>2.0.CO;2.

Bueh, C., N. Shi, and Z. Xie, 2011: Large-scale circulation anomalies associated with persistent low temperature over southern China in January 2008. *Atmos. Sci. Lett.*, **12**, 273–280, doi:10.1002/asl.333.

Cohen, J., J. C. Furtado, M. A. Barlow, V. A. Alexeev, and J. E. Cherry, 2012: Arctic warming, increasing snow cover and widespread boreal winter cooling. *Environ. Res. Lett.*, **7**, 014007, doi:10.1088/1748-9326/7/1/014007.

——, and Coauthors, 2014: Recent arctic amplification and extreme mid-latitude weather. *Nat. Geosci.*, **7**, 627–637, doi:10.1038/ngeo2234.

Comiso, J. C., C. L. Parkinson, R. Gersten, and L. Stock, 2008: Accelerated decline in the arctic sea ice cover. *Geophys. Res. Lett.*, **35**, L01703, doi:10.1029/2007GL031972.

Czaja, A., and C. Frankignoul, 2002: Observed impact of Atlantic SST anomalies on the North Atlantic Oscillation. *J. Climate*, **15**, 606–623, doi:10.1175/1520-0442(2002)015<0606:OIOASA>2.0.CO;2.

Dee, D. P., and Coauthors, 2011: The ERA-Interim reanalysis: Configuration and performance of the data assimilation system. *Quart. J. Roy. Meteor. Soc.*, **137**, 553–597, doi:10.1002/qj.828.

Han, Z., S. Li, and M. Mu, 2011: The role of warm North Atlantic SST in the formation of positive height anomalies over the Ural Mountains during January 2008. *Adv. Atmos. Sci.*, **28**, 246–256, doi:10.1007/s00376-010-0069-1.

Holopainen, E. O., and C. Fortelius, 1987: High-frequency transient eddies and blocking. *J. Atmos. Sci.*, **44**, 1632–1645, doi:10.1175/1520-0469(1987)044<1632:HFTEAB>2.0.CO;2.

——, L. Rontu, and N. C. Lau, 1982: The effect of large-scale transient eddies on the time-mean flow in the atmosphere. *J. Atmos. Sci.*, **39**, 1972–1984, doi:10.1175/1520-0469(1982)039<1972:TEOLST>2.0.CO;2.

Honda, M., J. Inoue, and S. Yamane, 2009: Influence of low arctic sea-ice minima on anomalously cold Eurasian winters. *Geophys. Res. Lett.*, **36**, L08707, doi:10.1029/2008GL037079.

Hori, M. E., J. Inoue, T. Kikuchi, M. Honda, and Y. Tachibana, 2011: Recurrence of intraseasonal cold air outbreak during the 2009/2010 winter in Japan and its ties to the atmospheric condition over the Barents-Kara Sea. *SOLA*, **7**, 25–28, doi:10.2151/sola.2011-007.

Hoskins, J. B., and T. Ambrizzi, 1993: Rossby wave propagation on a realistic longitudinally varying flow. *J. Atmos. Sci.*, **50**, 1661–1671, doi:10.1175/1520-0469(1993)050<1661:RWPOAR>2.0.CO;2.

——, I. N. James, and G. H. White, 1983: The shape, propagation and mean-flow interaction of large-scale weather

systems. *J. Atmos. Sci.*, **40**, 1595–1612, doi:10.1175/1520-0469(1983)040<1595:TSPAMF>2.0.CO;2.

Inoue, J., M. E. Hori, and K. Takaya, 2012: The role of Barents Sea ice in the wintertime cyclone track and emergence of a warm-arctic cold-Siberian anomaly. *J. Climate*, **25**, 2561–2568, doi:10.1175/JCLI-D-11-00449.1.

Lau, N.-C., 1988: Variability of the observed midlatitude storm tracks in relation to low-frequency changes in the circulation pattern. *J. Atmos. Sci.*, **45**, 2718–2743, doi:10.1175/1520-0469(1988)045<2718:VOTOMS>2.0.CO;2.

——, and E. O. Holopainen, 1984: Transient eddy forcing of the time-mean flow as identified by geopotential tendencies. *J. Atmos. Sci.*, **41**, 313–328, doi:10.1175/1520-0469(1984)041<0313:TEFOTT>2.0.CO;2.

Lim, Y. K., 2015: The east Atlantic/west Russia (EA/WR) teleconnection in the North Atlantic: Climate impact and relation to Rossby wave propagation. *Climate Dyn.*, **44**, 3211–3222, doi:10.1007/s00382-014-2381-4.

Liu, J., J. A. Curry, H. Wang, M. Song, and R. M. Horton, 2012: Impact of declining arctic sea ice on winter snowfall. *Proc. Natl. Acad. Sci. USA*, **109**, 4074–4079, doi:10.1073/pnas.1114910109.

Luo, D., A. Lupo, and H. Wan, 2007: Dynamics of eddy-driven low-frequency dipole modes. Part I: A simple model of North Atlantic Oscillations. *J. Atmos. Sci.*, **64**, 3–38, doi:10.1175/JAS3818.1.

——, L. Zhong, R. Ren, and C. Wang, 2010: Spatial pattern and zonal shift of the North Atlantic Oscillation. Part II: Numerical experiments. *J. Atmos. Sci.*, **67**, 2827–2853, doi:10.1175/2010JAS3340.1.

——, Y. Yao, and A. Dai, 2015a: Decadal relationship between European blocking and the North Atlantic Oscillation during 1978–2011. Part I: Atlantic conditions. *J. Atmos. Sci.*, **72**, 1152–1173, doi:10.1175/JAS-D-14-0039.1.

——, ——, and ——, 2015b: Decadal relationship between European blocking and North Atlantic Oscillation during 1978–2011. Part II: A theoretical model study. *J. Atmos. Sci.*, **72**, 1174–1199, doi:10.1175/JAS-D-14-0040.1.

——, Y. Xiao, Y. Yao, A. Dai, I. Simmonds, and C. Franzke, 2016: Impact of Ural blocking on winter warm Arctic–cold Eurasian anomalies. Part I: Blocking-induced amplification. *J. Climate*, **29**, 3925–3947, doi:10.1175/JCLI-D-15-0611.1.

Mori, M., M. Watanabe, H. Shiogama, J. Inoue, and M. Kimoto, 2014: Robust arctic sea-ice influence on the frequent Eurasian cold winters in past decades. *Nat. Geosci.*, **7**, 869–873, doi:10.1038/ngeo2277.

Nakamura, H., M. Nakamura, and J. L. Anderson, 1997: The role of high- and low-frequency dynamics in the blocking formation. *Mon. Wea. Rev.*, **125**, 2074–2093, doi:10.1175/1520-0493(1997)125<2074:TROHAL>2.0.CO;2.

Newson, R. L., 1973: Response of general circulation model of the atmosphere to removal of the arctic ice cap. *Nature*, **241**, 39–40, doi:10.1038/241039b0.

Overland, J., K. R. Wood, and M. Wang, 2011: Warm Arctic-cold continents: Climate impacts of the newly open Arctic Sea. *Polar Res.*, **30**, 15787, doi:10.3402/polar.v30i0.15787.

Peings, Y., and G. Magnusdottir, 2014: Response of the wintertime Northern Hemisphere atmospheric circulation to current and projected arctic sea ice decline: A numerical study with CAM5. *J. Climate*, **27**, 244–264, doi:10.1175/JCLI-D-13-00272.1.

Petoukhov, V., and V. A. Semenov, 2010: A link between reduced Barents-Kara sea ice and cold winter extremes over northern continents. *J. Geophys. Res.*, **115**, D21111, doi:10.1029/2009JD013568.

Rudeva, I., and I. Simmonds, 2015: Variability and trends of global atmospheric frontal activity and links with large-scale modes of variability. *J. Climate*, **28**, 3311–3330, doi:10.1175/JCLI-D-14-00458.1.

Sato, K., J. Inoue, and M. Watanabe, 2014: Influence of the Gulf Stream on the Barents Sea ice retreat and Eurasian coldness during early winter. *Environ. Res. Lett.*, **9**, 084009, doi:10.1088/1748-9326/9/8/084009.

Screen, J. A., and I. Simmonds, 2010: The central role of diminishing sea ice in recent arctic temperature amplification. *Nature*, **464**, 1334–1337, doi:10.1038/nature09051.

——, and ——, 2013a: Exploring links between arctic amplification and mid-latitude weather. *Geophys. Res. Lett.*, **40**, 959–964, doi:10.1002/grl.50174.

——, and ——, 2013b: Caution needed when linking weather extremes to amplified planetary waves. *Proc. Natl. Acad. Sci. USA*, **110**, E2327, doi:10.1073/pnas.1304867110.

——, and ——, 2014: Amplified mid-latitude planetary waves favour particular regional weather extremes. *Nat. Climate Change*, **4**, 704–709, doi:10.1038/nclimate2271.

Simmonds, I., and K. Keay, 2002: Surface fluxes of momentum and mechanical energy over the North Pacific and North Atlantic Oceans. *Meteor. Atmos. Phys.*, **80**, 1–18, doi:10.1007/s007030200009.

——, and P. D. Govekar, 2014: What are the physical links between arctic sea ice loss and Eurasian winter climate? *Environ. Res. Lett.*, **9**, 101003, doi:10.1088/1748-9326/9/10/101003.

Takaya, K., and H. Nakamura, 2001: A formulation of a phase-independent wave-activity flux for stationary and migratory quasigeostrophic eddies on a zonally varying basic flow. *J. Atmos. Sci.*, **58**, 608–627, doi:10.1175/1520-0469(2001)058<0608:AFOAPI>2.0.CO;2.

Tang, Q., X. Zhang, X. Yang, and J. A. Francis, 2013: Cold winter extremes in northern continents linked to arctic sea ice loss. *Environ. Res. Lett.*, **8**, 014036, doi:10.1088/1748-9326/8/1/014036.

Tibaldi, S., and F. Molteni, 1990: On the operational predictability of blocking. *Tellus*, **42A**, 343–365, doi:10.1034/j.1600-0870.1990.t01-2-00003.x.

Walsh, J. E., 2014: Intensified warming of the Arctic: Causes and impacts on middle latitudes. *Global Planet. Change*, **117**, 52–63, doi:10.1016/j.gloplacha.2014.03.003.

Wen, M., S. Yang, A. Kumar, and P. Zhang, 2009: An analysis of the large-scale climate anomalies associated with the snowstorms affecting China in January 2008. *Mon. Wea. Rev.*, **137**, 1111–1131, doi:10.1175/2008MWR2638.1.

Zhang, X., C. Lu, and Z. Guan, 2012: Weakened cyclones, intensified anticyclones and recent extreme cold winter weather events in Eurasia. *Environ. Res. Lett.*, **7**, 044044, doi:10.1088/1748-9326/7/4/044044.